Examining Atmospheric River Life Cycles in East Antarctica

Jonathan Wille[1], Benjamin Pohl[2], Vincent Favier[3], Andrew Winters[4], Rebecca Baiman[4], Steven Cavallo[5], Christophe Leroy-Dos Santos[6], Kyle R Clem[7], Danielle G Udy[8], Tessa Rosemary Vance[9], Irina Gorodetskaya[10], Francis Codron[11], and Antoine Berchet[12]

[1]ETH Zurich
[2]CRC / Biogéosciences
[3]Université Grenoble Alpes - CNRS
[4]University of Colorado Boulder
[5]University of Oklahoma
[6]Laboratoire des Sciences du Climat et de l'Environnementf
[7]Victoria University of Wellington
[8]University of Tasmania
[9]Antarctic Climate & Ecosystems Cooperative Research Centre
[10]University of Porto
[11]LOCEAN, Sorbonne Université/CNRS/IRD/MNHN
[12]Laboratoire des Sciences du Climat et de l'Environnement, CEA-CNRS-UVSQ

September 11, 2023

Abstract

During atmospheric river (AR) landfalls on the Antarctic ice sheet, the high waviness of the circumpolar polar jet stream allows for sub-tropical air masses to be advected towards the Antarctic coastline. These rare but high-impact AR events are highly consequential for the Antarctic mass balance; yet little is known about the various atmospheric dynamical components determining their life cycle. By using an AR detection algorithm to retrieve AR landfalls at Dumont d'Urville and non-AR analogues based on 700 hPa geopotential height, we examined what makes AR landfalls unique and studied the complete life cycle of ARs to affect Dumont d'Urville. ARs form in the mid-latitudes/sub-tropics in areas of high surface evaporation, likely in response to tropical deep convection anomalies. These convection anomalies likely lead to Rossby wave trains that help amplify the upper-tropospheric flow pattern. As the AR approaches Antarctica, condensation of isentropically lifted moisture causes latent heat release that – in conjunction with poleward warm air advection – induces geopotential height rises and anticyclonic upper-level potential vorticity tendencies downstream. As evidenced by a blocking index, these tendencies lead to enhanced ridging/blocking that persist beyond the AR landfall time, sustaining warm air advection onto the ice sheet. Finally, we demonstrate a connection between tropopause polar vortices and mid-latitude cyclogenesis in an AR case study. Overall, the non-AR analogues reveal that the amplified jet pattern observed during AR landfalls is a result of enhanced poleward moisture transport and associated diabatic heating which is likely impossible to replicate without strong moisture transport.

Hosted file

`973498_0_art_file_11364409_s0lbnj.docx` available at https://authorea.com/users/602812/articles/664291-examining-atmospheric-river-life-cycles-in-east-antarctica

Hosted file

973498_0_supp_11364410_s0jbnk.docx available at https://authorea.com/users/602812/articles/664291-examining-atmospheric-river-life-cycles-in-east-antarctica

Examining Atmospheric River Life Cycles in East Antarctica

Jonathan D. Wille[1,2*], Benjamin Pohl[3], Vincent Favier[1], Andrew C. Winters[4], Rebecca Baiman[4], Steven M. Cavallo[5], Christophe Leroy-Dos Santos[6], Kyle Clem[7], Danielle G Udy[8,9], Tessa R Vance[9], Irina Gorodetskaya[10], Francis Codron[11], Antoine Berchet[6]

[1] Institut des Géosciences de l'Environnement, CNRS/UGA/IRD/G-INP, Saint Martin d'Hères, France

[2] Institute for Atmospheric and Climate Science, ETH Zurich, Zurich, Switzerland

[3] Biogéosciences, CNRS / Université de Bourgogne Franche-Comté, Dijon, France

[4] Department of Atmospheric and Oceanic Sciences, University of Colorado Boulder

[5] School of Meteorology, University of Oklahoma

[6] Laboratoire des Sciences du Climat et de l'Environnement, Gif-Sur-Yvette, France

[7] School of Geography, Environment and Earth Sciences, Victoria University of Wellington, New Zealand

[8] Institute for Marine & Antarctic Studies, University of Tasmania, Hobart, Tasmania 7004, Australia

[9] Australian Antarctic Program Partnership, Institute for Marine & Antarctic Studies, University of Tasmania, Hobart, Tasmania 7004, Australia

[10] CIIMAR - Interdisciplinary Centre of Marine and Environmental Research of the University of Porto, Portugal

[11] Laboratoire d'Océanographie et du Climat, LOCEAN-IPSL, Sorbonne Université, CNRS, IRD, MNHN, Paris 75252, France

Corresponding author: Jonathan Wille (jonathan.wille@env.ethz.ch)

Key Points:

- Atmospheric rivers have lower-latitude moisture sources than most extratropical cyclones, and are influenced by tropopause polar vortices
- Large latent heat release of the atmospheric river moisture transport leads to downstream anticyclonic potential vorticity tendencies
- Large latent heat release and diabatic heating helps maintain atmospheric blocking after an atmospheric river has dissipated

Abstract

During atmospheric river (AR) landfalls on the Antarctic ice sheet, the high waviness of the circumpolar polar jet stream allows for subtropical air masses to be advected towards the Antarctic coastline. These rare but high-impact AR events are highly consequential for the Antarctic mass balance; yet little is known about the various atmospheric dynamical components determining their life cycle. By using an AR detection algorithm to retrieve AR landfalls at Dumont d'Urville and non-AR analogues based on 700 hPa geopotential height, we examined what makes AR landfalls unique and studied the complete life cycle of ARs to affect Dumont d'Urville. ARs form in the mid-latitudes/subtropics in areas of high surface evaporation, likely in response to tropical deep convection anomalies. These convection anomalies likely lead to Rossby wave trains that help amplify the upper-tropospheric flow pattern. As the AR approaches Antarctica, condensation of isentropically lifted moisture causes latent heat release that – in conjunction with poleward warm air advection – induces geopotential height rises and anticyclonic upper-level potential vorticity tendencies downstream. As evidenced by a blocking index, these tendencies lead to enhanced ridging/blocking that persist beyond the AR landfall time, sustaining warm air advection onto the ice sheet. Finally, we demonstrate a connection between tropopause polar vortices and mid-latitude cyclogenesis in an AR case study. Overall, the non-AR analogues reveal that the amplified jet pattern observed during AR landfalls is a result of enhanced poleward moisture transport and associated diabatic heating which is likely impossible to replicate without strong moisture transport.

Plain Language Summary

When the polar jet stream that surrounds Antarctica is highly wavy, air masses from the subtropics that are warm and humid are often transported over the ice sheet in the form of atmospheric rivers (ARs). When ARs reach Antarctica, they often bring extreme weather conditions that have large consequences for ice sheet snowfall and surface melt. Here we studied the full life cycle of ARs that reached Dumont d'Urville in East Antarctica and compare these ARs against events with similar profiles of atmospheric circulation. ARs typically form in areas of unusually high surface evaporation and thunderstorm convection in the subtropics. This convection sends Rossby waves towards the Antarctic coastline which help make the polar jet wavier. The amplitude of the polar jet is further enhanced when the moisture that accompanies the ARs condensates over the cooler seas around Antarctica and creates large latent heating. The higher amplitude of the polar jet often results in atmospheric blocks that transports further warm, moist air over the ice sheet even after the AR has made landfall and dissipated. Therefore, extreme weather events over Antarctica like ARs are sensitive to climate changes far from the continent over the subtropical regions.

1 Introduction

Under a favorable polar jet pattern, atmospheric rivers (ARs) over the Southern Ocean advect moist subtropical / mid-latitude air masses poleward towards the Antarctic continent in association with successive mesoscale frontal waves. These ARs serve as a major conduit of air mass transport from the humid, warmer subtropics and mid-latitudes to the polar desert Antarctic Ice Sheet (AIS). These filaments of intense poleward moisture transport are typically associated with a low-level jet ahead of an extratropical cyclone's cold front in a similar position as the warm conveyor belt (Harrold, 1973; Madonna et al., 2014; Nash et al., 2018; Ralph et al., 2004; Sinclair & Dacre, 2019; Zhu & Newell, 1998). In general, ARs act as rare but high impact events for the AIS mass balance, as they have been linked to surface melting on the West Antarctic Ice Sheet (Adusumilli et al., 2021; Benedict et al., 2019; M. L. Maclennan et al., 2023; Martin et al., 2019; Sodemann & Stohl, 2013; Wille et al., 2019, 2021, 2022), record-high temperatures (Bozkurt et al., 2018; González-Herrero et al., 2022; Gorodetskaya et al., 2023; Turner et al., 2022; Xu et al., 2021, Wille et al., 2023a), extreme snowfall events (Adusumilli et al., 2021; Gehring et al., 2022; Gorodetskaya et al., 2014; Maclennan et al., 2022; Simon et al., 2023; Wille et al., 2021, Wille et al., 2023b), and sea-ice decline in marginal ice zones (Liang et al., 2023). Additionally, ARs have been shown to promote ice shelf instability that can lead to their collapse on the Antarctic Peninsula (Wille et al., 2022). Overall, ARs are a net positive for the Antarctic surface mass balance and have the potential to partly mitigate the AIS contribution to sea level rise through enhanced precipitation over Eastern Antarctica (Favier et al., 2017; Kittel et al., 2021; Ligtenberg et al., 2013; Mottram et al., 2021; Rignot et al., 2019). However, they could become a net negative for mass balance, like in Greenland, if the Antarctic climate warms (Mattingly et al., 2023), given the future projections of Antarctic climate warming (Gutierrez et al., 2021). Thus, understanding the dynamics that embodies an AR is crucial for predicting how weather extremes in the Antarctic and their impacts will change in response to not only high-latitude climate changes, but also climate changes at the more humid low-latitudes.

Conditions far from the Antarctic continent over the warmer mid-latitudes and subtropics play a vital role in shaping AR intensity over Antarctica. Deep convection over the tropical central Pacific has been shown to trigger Rossby wave trains that allow ARs to reach the Antarctic Peninsula during summer (Clem et al., 2022; Gorodetskaya et al., 2023). Meanwhile, a recent extreme AR event over East Antarctica that set a new maximum temperature record at the Dome C and Vostok stations originated from the moisture reservoirs of multiple tropical cyclones while other convective anomalies in the central Indian Ocean triggered a Rossby wave train directed toward the East Antarctic coastline (Wille et al., 2023a). Terpstra et al (2021) examined the origins of an AR that brought anomalous snowfall to Dronning Maud Land (DML, East Antarctica) in February 2011 stipulating that AR air parcels initially gathered moisture through surface evaporation in the subtropics and then lost moisture when they moved over colder sea surface temperatures and in response to the isentropic ascent. Additional horizontal moisture convergence in the mid-latitudes occurred during mesocyclone development near the coast of Antarctica re-enhancing precipitation over DML. The horizontal moisture convergence could not compensate for the moisture loss via precipitation, and the moisture maximum vertically separated from the low-level jet near the surface.

This initial moisture transport from the mid-latitudes and subtropics often aids in the explosive cyclogenesis of cyclones already formed and traversing the mid-latitudes of the Southern Ocean, but not necessarily the initial cyclogenesis of poleward-bound cyclones (Zhu & Newell, 1994). One potential source of surface cyclogenesis are tropopause polar vortices (TPVs) which are defined by a potential temperature minimum and potential vorticity (PV) maximum on the dynamic tropopause, as well as a lower tropopause height in the cyclone's cold sector (Cavallo & Hakim, 2010; Hakim, 2000). When TPVs move over regions of enhanced low-level baroclinicity, they often trigger cyclogenesis through the enhancement of potential vorticity near the tropopause and have been linked to extreme weather events in the Northern Hemisphere mid-latitudes and Rossby wave initiation events (Bray & Cavallo, 2022; Cavallo & Hakim, 2009; Hoskins et al., 1985; Lillo et al., 2021; Röthlisberger et al., 2018), even though their relation with ARs has never been explored. The TPVs, which sometimes have lifetimes of several months, are maintained by a combination of clear-sky radiative cooling over an ice surface and cloud-top radiative cooling (Cavallo & Hakim, 2009, 2013). The high values of radiative cooling over the AIS and topography that impedes intrusions of the polar jet makes it an ideal location for TPV formation (Gordon et al., 2022), with 56.2% of Antarctic surface cyclones associated with a TPV at some point in their lifetime. In contrast, the incidence of TPVs is generally independent of Antarctic surface cyclones, with only 3.6% of TPVs associated with cyclones (Gordon et al., 2022). Thus TPVs frequently influence cyclones, but not the other way around. Given the precursory role that TPVs play in extratropical cyclogenesis, and the connection of ARs with extratropical cyclones, a logical step is to see if there is a link between TPVs and Antarctic AR behavior.

Moreover, intense cyclogenesis is insufficient to promote poleward-oriented ARs. Most moisture transport in the Southern Ocean is zonal in alignment with the climatological structure of the polar jet stream (Simmonds et al., 2003). Deviations in the waviness of the polar jet and its hemispheric symmetry contribute to the propensity for extra-tropical cyclones to reach the Antarctic coastline instead of circumnavigating the Southern Ocean as per usual (Hoskins & Hodges, 2005; King & Turner, 2007; Simmonds et al., 2003). Indeed, the highest precipitation events over the AIS tend to occur when the mid-tropospheric jet is in a highly amplified pattern (Hirasawa et al., 2013; Michelle L. Maclennan & Lenaerts, 2021; Massom et al., 2004; Schlosser et al., 2010; Scott et al., 2019; Sinclair & Dacre, 2019). However, the cause of the very amplified polar jet often observed during large poleward moisture transport events is still unclear. During notable AR events that generated large precipitation and high temperature anomalies across the AIS, a perturbed jet pattern with strong downstream ridging was always present (Bozkurt et al., 2018; Gorodetskaya et al., 2023; I. V. Gorodetskaya et al., 2014; Nicolas & Bromwich, 2011; Terpstra et al., 2021; Turner et al., 2022; Wille et al., 2019, 2022). While the persistence of the ridging in regard to blocking (i.e. sustained ridge for 4-5 days) was not often considered, one study highlighted a blocking pattern as favorable for the development of an “AR family” event (Maclennan et al., 2023). While atmospheric ridging/blocking is a prerequisite for ARs to reach the AIS, the presence of strong ridging/blocking does not guarantee an AR occurrence (Pohl et al., 2021; Wille et al., 2021). For instance, particular weather regimes with strong ridging/blocking that favor AR landfalls in Adélie Land were identified by Pohl et al., 2021. However, within these weather regimes, AR landfall events only accounted for roughly 6-13% of the total days mapping to those regimes, and had higher geopotential height anomalies compared to non-AR days within the same regime. These statistics demonstrate that ridging/blocking does not ensure an AR landfall and that some unaccounted for processes were amplifying the ridging during AR events relative to non-AR days (Pohl et al., 2021). A challenge is to better identify atmospheric blocking around Antarctica and determine the influence of ARs on blocking formation/persistence.

In an AR case study over East Antarctica, Terpstra et al.(2021) showed that the poleward transport of heat and moisture released latent heat through condensation/deposition, thus increasing the diabatic heating and the intensity of vertical motion based on quasigeostrophic theory (Bluestein, 1992). Latent heat release occurred as air parcels were lifted along isentropic surfaces promoting their condensation while the air mass pathway over cooler sea surface temperatures suppressed surface evaporation. Plus, as seen with the AR event studied in Terpstra et al., (2021) and seen with most austral winter extratropical cyclones, the systems with the largest poleward propagation speeds deliver 2.5 times more moisture transport towards the Antarctic coastline and often resemble open frontal waves (Sinclair & Dacre, 2019). These increased poleward propagation speeds are linked to lower-level cyclonic PV tendencies caused by the resulting diabatic heating from enhanced latent heat release (Tamarin & Kaspi, 2016). Thus, it is prudent to investigate how the latent heat release associated with poleward AR transport influences the upper-level PV and downstream ridging.

Overall, ARs represent a teleconnection where changes in the Southern Hemisphere subtropical/mid-latitude climate can directly translate to changes in AIS mass balance. This study aims to increase our comprehension of AR dynamics over Antarctica by examining ARs from genesis to landfall. Here, we examine the full life cycle of ARs impacting a location around Dumont d'Urville (DDU henceforth) station, in Adélie Land region, on East Antarctica, to determine what makes them unique in terms of attendant cyclogenesis and tropical moisture export, how the polar jet influences and responds to the moisture transport within ARs, and how this evolution influences downstream atmospheric ridging and blocking once an AR reaches the coastline. Particularly, we analyzed the following:

- Determining the differences in AR genesis locations between AR and non-AR atmospheric circulation analogues using back trajectories
- Comparing the synoptic differences of ARs and their non-AR analogues in the days prior to their landfall
- Examining the potential vorticity tendencies from diabatic heating related to AR-related moisture condensation and deposition
- Using a blocking-index to quantify AR relationships with atmospheric blocking
- Studying an AR case study, in which we examine the relationship between the AR and TPVs

2 Data and Methods

2.1 The atmospheric river detection scheme

We employ the AR detection algorithm described in Wille et al. (2021) to search for ARs from January 1980 - December 2020. This algorithm searches for grid cells between 37.5°S and 85°S where the meridional (v) component of integrated vapor transport (vIVT) exceeds the 98th percentile of all monthly vIVT values. The same is also done using integrated water vapor (IWV) to create a second catalog of AR detections. Using a relative threshold takes into account the progressive reduction of atmospheric saturation capacity moving poleward. Consecutive grid points above this threshold that extend at least 20° in the meridional direction are classified as ARs. Here, vIVT and IWV are defined as:

$$vIVT = -\frac{1}{g}\int_{surface}^{top} qvdp \quad (1)$$

$$IWV = -\frac{1}{g}\int_{surface}^{top} q dp \quad (2)$$

where g (m s^{-2}) is the gravitational acceleration, q (kg kg^{-1}) is the specific humidity, v is the meridional wind velocity (m s^{-1}), and p is the atmospheric pressure (hPa). vIVT and IWV are calculated using all reanalysis levels, from the surface to the top of the atmosphere. As previously done in Pohl et al., (2021), the two detection schemes are used to retrieve ARs that make landfall along the coastline around DDU between 138°E and 142°E. The data used to initialize the AR detection is provided by the Modern-Era Retrospective analysis for Research and Applications, Version 2 (MERRA-2), which has a 0.5° × 0.625° horizontal grid spacing (Gelaro et al., 2017). Using MERRA-2 (i) is standard for all AR detection algorithms that are part of the Atmospheric River Tracking Method Intercomparison Project (Rutz et al., 2019), and (ii) ensures independence between the weather and AR definitions, both in terms of algorithms and the input data set. Nonetheless, previous analysis has shown that when the AR detection algorithm is initialized with data from the ERA5 reanalysis, there is very little difference in AR detection frequency compared against MERRA-2 (Wille et al., 2021). The criteria for AR detection are stricter in this algorithm compared to global algorithms, as evidenced by the lower annual frequency of AR detections around the Antarctic coastline (1.2% and ~6%, respectively; Wille et al., 2021, Collow et al., 2022; Shields et al., 2022).

2.2 K-means clustering

Here, we re-use the partitioning into 15 weather regimes proposed and discussed in Pohl et al., (2021). These regimes are obtained through a k-means clustering of 700 hPa geopotential height (Z700) anomalies, after removing the mean annual cycle, as taken from ERA5 reanalysis, which has a horizontal resolution of 0.25° x 0.25°, during the period 1 January 1979 to 31 December 2018. Regimes were calculated over the domain 45°S-75°S, 110°E-170°E (corresponding to 121 x 241 grid-points), which is approximately centered on Adélie Land. Three regimes (namely, #9-10-11), promoting northerly flow from the mid-latitudes towards Antarctica, were identified as the most favorable conditions for AR development and landfall in Adélie Land (see Figure 2 in Pohl et al., 2021). These regimes are characterized by a high-pressure / positive geopotential anomaly located over the Southern Ocean, east of the DDU sector, and are horizontally juxtaposed with a low-pressure / negative geopotential anomaly farther west, similar to the weather types described in (Udy et al., 2021). Such a configuration produces northerly geostrophic wind that is favorable for advecting heat and moisture towards Antarctica. The same three regimes show more amplified synoptic configurations (that is, more intense negative, and even stronger positive anomalies, resulting in stronger northerly winds) when they co-occur with AR events (Pohl et al., 2021). However, Pohl et al., (2021) identified these unusually strong synoptic configurations as a necessary, but not a sufficient condition for ARs, since similar days are also observed during non-AR conditions. The reverse is less true, as all landfalling ARs are associated with strong atmospheric centers of action in the middle troposphere.

2.3 AR and non-AR analogues

In order to better identify what differentiates AR from non-AR days under similar synoptic conditions, we (i) extracted the 700 hPa geopotential height anomaly fields corresponding to each AR day over the same domain used in Pohl et al. (2021) to define the aforementioned weather regimes; (ii) we identified the most similar non-AR day to each AR day, by minimizing the Euclidean distance between their respective 700 hPa geopotential height anomaly fields. In order to ensure that we do not consider the two days before or after AR events, we excluded them from the potential catalog of non-AR days. This criteria ensures that each AR and non-AR day pair corresponds to different synoptic events that are separated by at least 3 days. This methodology enables us to obtain two samples of days of equal size (comprising 639 AR-analogue pairs for the vIVT detection scheme, and 472 for the IWV detection scheme; more AR detections occur with the vIVT scheme (Wille et al., 2021)), with very similar synoptic flow patterns. Our methodology is more strict than a random selection of days ascribed to the same weather regime, since the non-AR days selected are those that most closely resemble their AR counterparts. In practice, all identified non-AR days are ascribed to the same regime as their corresponding AR days.

2.4 Back trajectory calculation

For the AR days and corresponding non-AR analogues from 2019-2020, the origin of air masses were evaluated using the Lagrangian Particle Dispersion Model Flexpart 10 (https://doi.org/10.5194/gmd-12-4955-2019). Every 6-hours a batch (500) of neutral inert air tracer particles are randomly released from a volume (0.1° x 0.1° x 100 m) centered around DDU coordinates (140°E, 66.65°S) at an altitude of 3000 m.a.s.l. Flexpart is driven by meteorological fields from ERA5 (Hersbach et al., 2020) at 1°x1° horizontal resolution (downloaded using the flexextract tool, https://doi.org/10.5194/gmd-13-5277-2020) to compute 10-day back-trajectories. Finally, the calculation indicates the number of particles over the ten-days back-trajectory at each grid point.

2.5 Tropopause polar vortex identification

TPV tracks are generated using the TPVTrack (v1.0) software, described in detail by Szapiro & Cavallo (2018) and described in its application to Southern Hemisphere TPVs in Gordon et al., (2022). We briefly summarize its key aspects here for convenience. TPVs are identified by finding local minima for cyclones in potential temperature on the tropopause using a watershed basin technique, where TPVs are represented as spatial objects. Basins are defined by relative vorticity. TPV objects at each time step can therefore have irregular shapes, which is a general characteristic of tropopause features. The TPV objects are tracked over time using horizontal and vertical correspondences between time steps to create TPV tracks that also consider vortex splits and mergers. The TPV tracks used in this study are the same as those used in Gordon et al. (2022) for the Southern Hemisphere.

2.6 Atmospheric river diabatic heating contribution

The distribution of diabatic heating during each AR and non-AR analogue case is estimated as a residual of the thermodynamic energy equation following Ling & Zhang (2013) using data from the ERA5 reanalysis at 3-h intervals:

$$Q = \frac{T}{\theta}\left(\frac{\partial\theta}{\partial t} + u\frac{\partial\theta}{\partial x} + v\frac{\partial\theta}{\partial y} + \omega\frac{\partial\theta}{\partial p}\right.\quad(3)$$

where Q is the diabatic heating rate ($Q = \frac{\partial\theta}{\partial t}$), T is the temperature, θ is the potential temperature, p is pressure, and u, v, and ω are the three-dimensional components of the wind. For ARs, it is assumed that latent heating processes dominate over the effects of radiation and friction (e.g., Lackmann, 2002; Reeves & Lackmann, 2004). We also assume that, to first-order, the PV tendency can be approximated based on vertical gradients of the diabatic heating when viewed across a large sample of cases (e.g., Cavallo & Hakim, 2010; Lackmann, 2002). Therefore, we estimate the PV tendency during each AR and non-AR analogue case using the diabatic heating rate calculated in (3) as:

$$\frac{dP}{dt} \approx -g\eta\left(\frac{\partial Q}{\partial p}\right) \quad (4)$$

Where P is the Ertel potential vorticity (Ertel, 1942), g is the gravitational acceleration, and η is the vertical component of the absolute vorticity. Conceptually, Equation 4 reveals that areas of latent heat release within ARs are associated with a reduction of cyclonic PV above the heating anomaly, enabling upper-tropospheric ridge amplification. The diabatic heating rates and PV tendencies calculated for each AR and non-AR analogue case are subsequently composited over a spatial domain centered on DDU (10–90°S; 60-240°E) during a 48-h period centered on the time of each AR or non-AR analogue case.

2.7 Blocking index

The blocking index presented in this study is an adaptation of the blocking index described in Pook et al., 2013 (henceforth the Pook blocking index) which is a flow-based blocking index primarily used to describe mid-latitude atmospheric blocking to the south of Australia and New Zealand, with implications for the frequency and intensity of weather extremes across southern Australia. The Pook blocking index is based on the summation and subtraction of the geostrophic westerly wind component (U components) at 500 hPa for a range of latitudes. The U components are calculated from 5-day running means of geopotential height to ensure the block is a temporal stationary feature as opposed to a ridge. For this study, the Pook blocking index was adapted for use over Antarctica by shifting the calculation of the zonal geopotential wind further south and calculating the blocking index for all longitudes. Also to account for seasonal biases observed in (Pook et al., 2013), we used anomalies in the U components based on monthly mean values to calculate the blocking index which follows as:

$$BI = 0.5(U_{35} + U_{40} + U_{65} + U_{70} - U_{50} - U_{60} - 2U_{55}) \quad (5)$$

3 Results

3.1 Back trajectories and moisture origins

Generally, peak AR track density is observed over the lower latitude regions compared to the overall extra-tropical storm track around Antarctica (Wille et al., 2021). Individual AR landfalls along the Antarctic coastline can feature moisture source regions in both the subtropics and midlatitudes (Clem et al., 2022; Gorodetskaya et al., 2023; Terpstra et al., 2021; Wille et al., 2022). To further examine AR moisture source regions, back trajectories from ARs during 2019 and 2020 were compared with those from non-AR analogues during the same years (Figure 1). The back trajectories made it possible to trace the origins of particles that were at 1000 and 3000 m asl above DDU at the time of each AR event (or corresponding non-AR analogue). Although very similar situations prevail in terms of position and intensity of the high-low pressure dipole around Antarctica during AR and non-AR analogues, resulting in a similar meridional circulation across the Southern Ocean, the back-trajectories diverge rapidly at mid-latitudes for the two categories of events. Trajectories during non-AR analogues tend to follow pathways from the southern Indian Ocean between 45-60°S, whereas AR trajectories originate preferentially from the Great Australian Bight (30-45°S), thereby confirming the conclusions of Pohl et al. (2021) concerning the potential moisture source for ARs making landfall in Adélie Land. Knowing that the inclusion of meridional wind in the vIVT calculation could indirectly force the trajectories to preferentially originate from lower latitudes, ARs (and their non-AR analogues) were also selected using algorithms based on IWV values (Figures 1c and 1d). However, the results exhibit few differences, suggesting that the source region for trajectories is not sensitive to the choice of detection scheme.

On the other hand, we find that trajectory pathway differences are more significant when we focus on air parcels that terminate at 3000 m asl rather than at 1000 m asl. At 1000 m asl above DDU, the boundary layer is still under the influence of katabatic flow, which can be seen in the dispersion of the back-trajectory signal, with some trajectories originating over the continent (Figures 1a and 1c). This impact of the katabatic flow on the distribution of trajectories is present for both ARs and non-AR analogues, which blurs differences in the circulations farther upstream. However, the more marked difference at 3000 m asl between ARs and non-AR analogues proves that the moisture within the ARs reaching Antarctica resides primarily in the mid-troposphere when it approaches the continent due to the isentropic ascent (Figures 1b and 1d). In addition, the air parcels most often responsible for precipitation at DDU are located at 3000 m asl (Jullien et al., 2020).

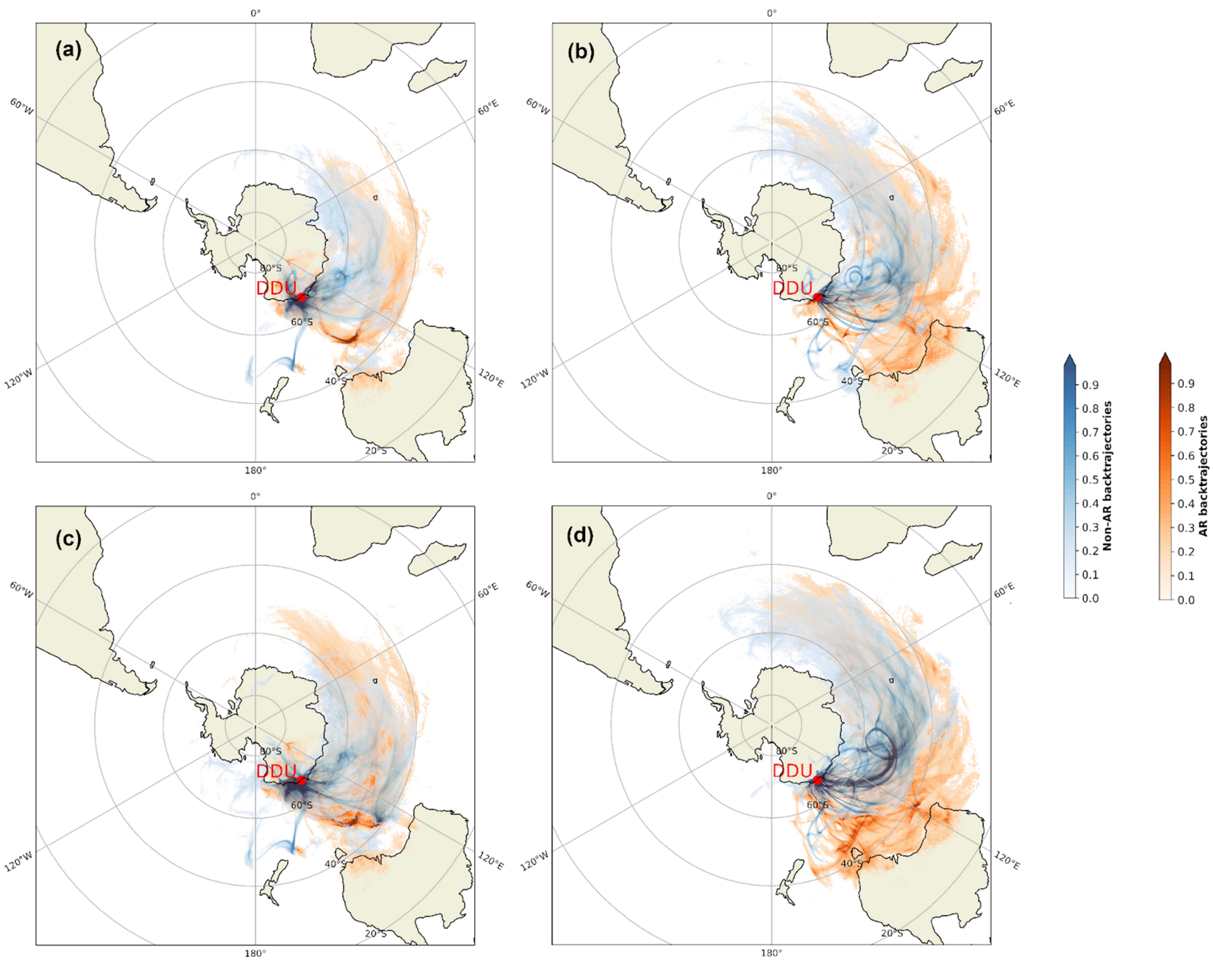

Figure 1. Figures showing the back trajectory analysis for all AR and non-AR analogues, 1000 m asl (a, c) and 3000m asl (b, d) according to the vIVT (a, b) and IWV (c, d) detection scheme.

When examining latent heat flux (LHF) anomalies from 1980-2020 during the four-day period prior to detected AR landfalls at DDU, a clear couplet of evaporation/negative LHF (blue) and condensation/positive LHF (red) is observed as the ARs move towards DDU (Figure 2a). Following the observations from Terpstra et al., (2021), most of the surface evaporation is found further north of the peak areas of condensation closer to the time of AR landfall, likely as a result of the prohibitively cooler ocean temperatures for evaporation. The difference between AR events and their non-AR analogues indicate that AR events have higher amounts of surface evaporation at lower latitudes (Figure 2b). There is a region of enhanced evaporation west of Australia 3-4 days prior to AR landfall that shifts farther eastward toward the southwest Australian coast from days -2 to 0 (landfall day). As seen in the case study of an AR influencing DML (Terpstra et al., 2021), during the ARs, the air masses arriving at higher altitudes at DDU (3 km vs 1 km) originate at much lower latitudes encompassing the southern Indian Ocean and the Great Australian Bight.

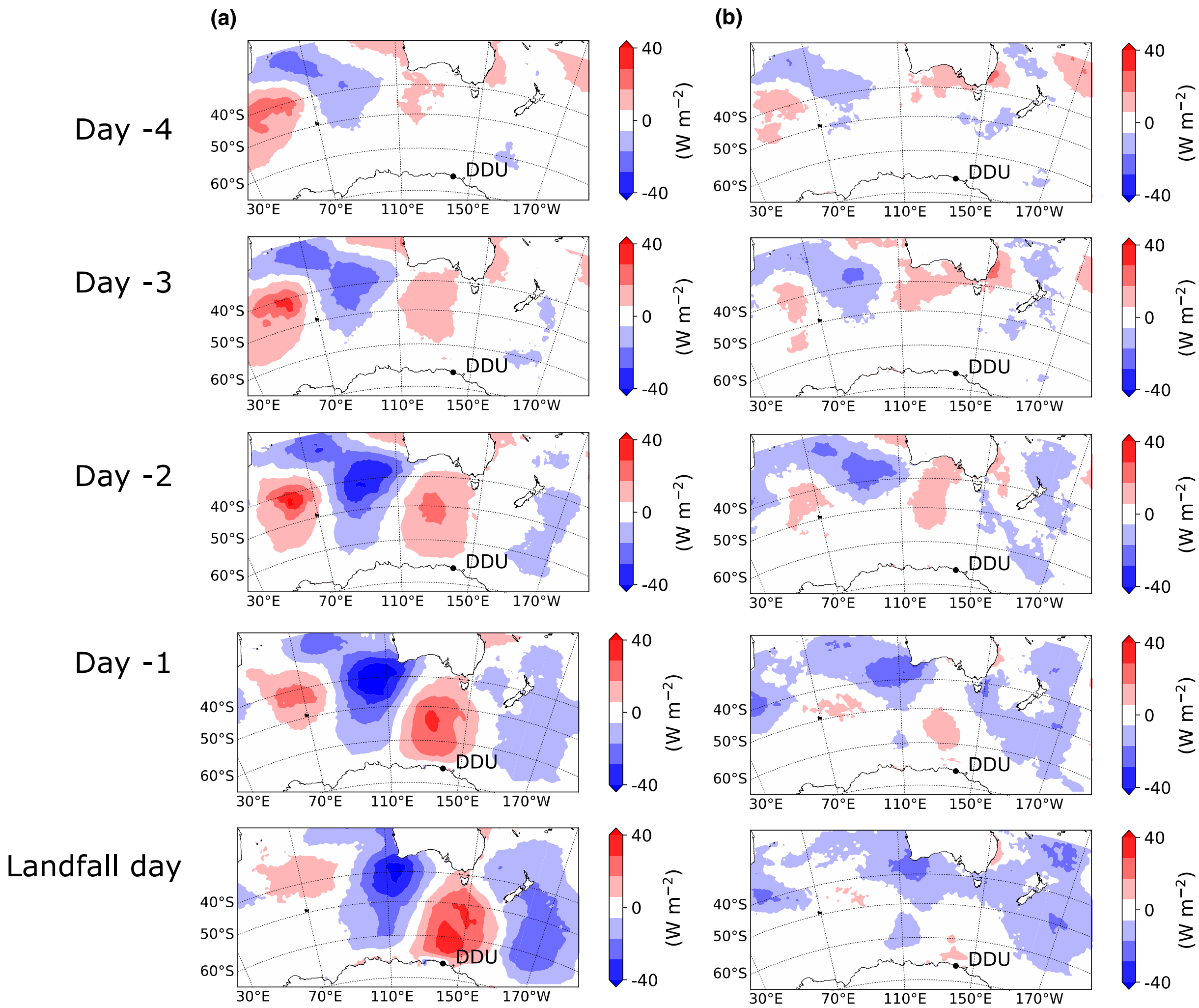

Figure 2. Composite daily surface latent heat flux anomalies for (a) atmospheric river landfalls and (b) difference between atmospheric rivers and their non-AR analogues around the DDU station. Areas of red represent greater condensation/heat exchange towards the surface or less evaporation/heat exchange towards the atmosphere than average and blue areas represent greater evaporation/heat exchange towards the atmosphere or less condensation/heat exchange towards the surface than average. Latent heat flux data was provided by ERA-5 reanalysis.

This enhanced lower-latitude evaporation becomes more evident when looking at Hovmöller diagrams of LHF anomalies averaged from -50° S to -20° S (Figures 3a-c) and from -70° S to -40° S (Figures 3d-f). The LHF anomalies are relatively similar between ARs and non-AR analogues within the -70° S to -40° S band, with ARs expectantly having more positive LHF anomalies around the time of landfall likely due to more intense precipitation (Figures 3d-f). The differences are more stark at lower latitudes within the -50° S to -20° S band, with AR events having a long span of negative LHF anomalies 10-20 W m^{-2} greater than the non-AR analogues in the central Indian Ocean during the -84 to +24 hour-period relative to AR landfall (Figure 3c). These larger negative LHF values indicate a greater moisture source for developing ARs compared to their analogues likely due to AR events occurring alongside areas of deep convection and large moisture reserves (Clem et al., 2022; Wille et al., 2023a).

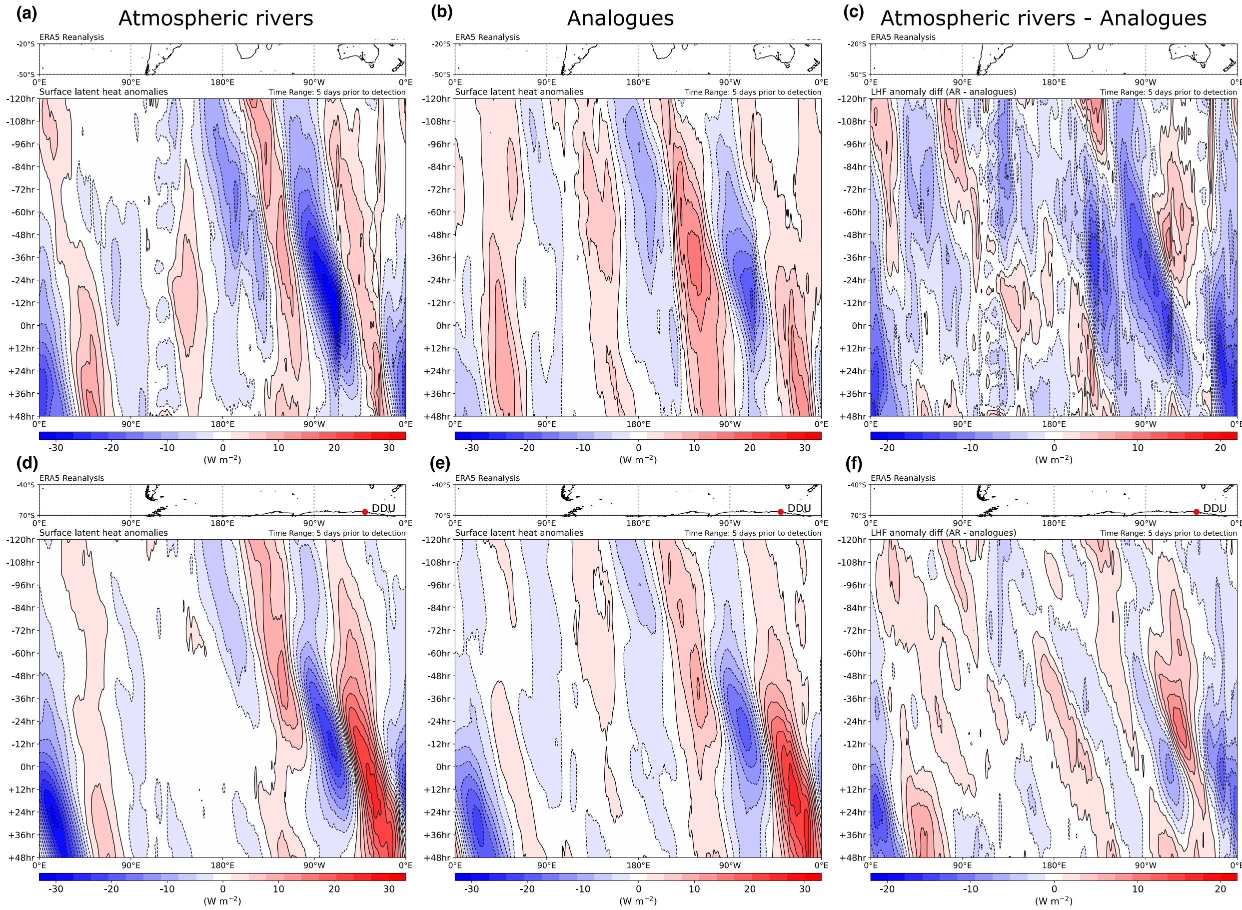

Figure 3. Composite Hovmoller diagram showing evolution of surface latent heat flux anomalies for (a,d) ARs, (b,e) non-AR analogues, and (c,f) their differences during the -5 to +2 days surrounding the AR landfall date at the DDU Station. Areas of red represent greater condensation/heat exchange towards the surface or less evaporation/heat exchange towards the atmosphere than average, and blue areas represent greater evaporation/heat exchange towards the atmosphere or less condensation/heat exchange towards the surface than average. 6-hourly surface latent heat flux data is averaged between(a-c) 20°S - 50°S and (d-f) 40°S - 70°S, and is provided by ERA-5 reanalysis.

3.2 Atmospheric river dynamics

The differences in ARs and non-AR analogues extend beyond the moisture source latitude. As seen before, the ARs that reach DDU are associated with large positive anomalies in 700 hPa geopotential height and northerly winds (Figures 4a and 4b). Meanwhile, the non-AR analogues, even though they are chosen because of their similarities with AR days, nonetheless show significant differences with respect to AR environments. The non-AR analogues feature geopotential and wind anomalies of the same sign, but at smaller magnitudes than AR days (Figures 4c, 4d, 4e, and 4f). This is especially true for the trough northwest of the AR, and for the ridge (or block) east of it. As a consequence, the low-high couplet that constitutes the typical environment in which Antarctic ARs develop (Pohl et al. 2021) is significantly weaker for non-AR analogues compared to AR days, thereby inducing weaker geostrophic flow and slower poleward transport allowing for more modification of the air mass by colder/drier ambient environment (Figure S1c). These differences suggest that, statistically speaking, ARs tend to show unique atmospheric circulation patterns that even the most similar non-AR days cannot reproduce. When looking at the days preceding AR landfalls at DDU, a distinct wavelike anomaly pattern in the 700 hPa geopotential height field is apparent until 3 days prior to landfall on average (Figure S2a). But when compared to the non-AR analogues, AR days show a much more amplified Rossby wave pattern (Figure S2b). The 700 hPa geopotential height anomalies are consistent with often observed PV anomalies in the upper-atmosphere which we explore further to verify this connection.

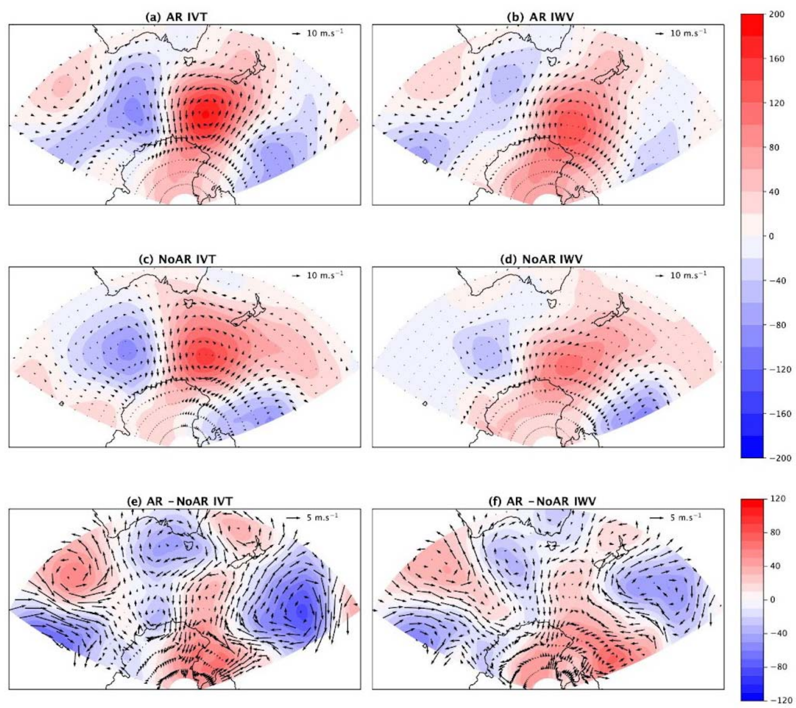

Figure 4. Geopotential height and wind vector anomalies at 700 hPa during AR and non-AR analogues, and their corresponding differences (AR - non-AR), for the vIVT (left) and IWV (right) detection schemes.

Looking at the time-evolution of the PV anomalies along the 320-K isentropic surface reveals a strong, prolonged response in the height of the dynamic tropopause in response to AR events at DDU. ARs and non-AR analogues both demonstrate wave-like PV anomalies on the 320-K isentrope (Figure 5). Interestingly, the maximum PV anomalies in both cases occur 12-24 hours after the time of AR landfall at DDU, demonstrating a pronounced influence of these flow patterns on the intensity of the upper-level downstream ridge long after the event has concluded. The main difference between the ARs and their non-AR analogues is the magnitude of these positive PV anomalies in the hours following the AR landfall, with the AR dates showing anomalies around 1 potential vorticity units greater than the non-AR analogues (Figure 5c). In addition to the increased positive PV anomalies, there is a westward shift in the peak AR related PV anomalies compared to their non-AR analogues, which suggests differences in the downstream propagation of wave energy between the two categories. The minima and maxima

PV anomalies for non-AR analogues are more horizontally stacked within the diagram, which implies a faster group velocity in these cases (Figures 5a and 5b). The slower group velocity for AR events is potentially indicative of the presence of high-latitude blocking during AR events, which could favor repeated AR landfalls in short succession (e.g., Hauser et al., 2023; Maclennan et al., 2023; Nakamura & Huang, 2018, and references therein).

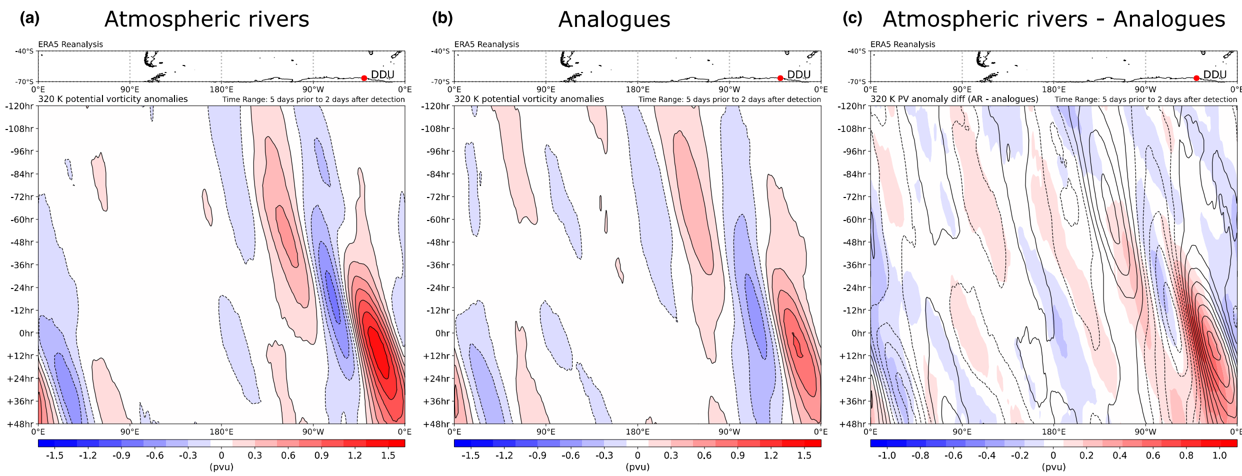

Figure 5. Composite Hovmoller diagram showing evolution of 320 K potential vorticity anomalies for (a) ARs, (b) non-AR analogues, and (c) their differences during the -5 to +2 day period surrounding AR landfall at DDU Station. For (c), the contours represent the non-AR analogues and the shading is the difference between the ARs and non-AR analogues. 6-hourly potential vorticity data is averaged between 40°S - 70°S and is provided by ERA-5 reanalysis

Figure 6 reveals that the composite evolutions of PV and diabatic heating for AR and non-AR analogue events are both characterized by an amplified upper-tropospheric flow pattern, with a trough located upstream of DDU and a ridge downstream of DDU. The trough during AR events is characterized by larger cyclonic PV values compared to the non-AR analogues, and it extends farther equatorward (Figures 6g–i). The larger cyclonic PV values associated with AR cases may highlight the cumulative influence of TPVs during AR cases, while the equatorward extension of the trough during AR cases reveals a greater potential for moisture advection from subtropical latitudes compared to the non-AR analogues.

The eastern flank of the upper-tropospheric trough, which coincides with the position of the AR during AR cases, features stronger 600 hPa diabatic heating rates compared to the non-AR analogues, together with larger anticyclonic PV tendencies at 400 hPa (Figures 6a–f). The larger anticyclonic PV tendencies align well with the apex of the upper-tropospheric ridge downstream of DDU in the AR case composite, suggesting that the ridge downstream of DDU is more amplified compared to the non-AR analogues. This is likely due to a greater 3D advection of PV related to the Rossby stationary wave fluxes transporting AR moisture poleward and the greater diabatic heating that results from this AR moisture condensing at higher latitudes causing larger latent heat release (Figures 6g–i; Zhang & Wang, 2018). This effect is further apparent when examining 700 hPa geopotential height gradients for ARs and non-AR analogues within the AR-favorable weather regimes identified in Pohl et al., (2021). As expected, the AR events have a larger geopotential height gradient compared to the non-AR analogues, with this strong gradient primarily driven by stronger downstream ridging during AR events rather than differences in the intensity of upstream troughs (Figure S1).

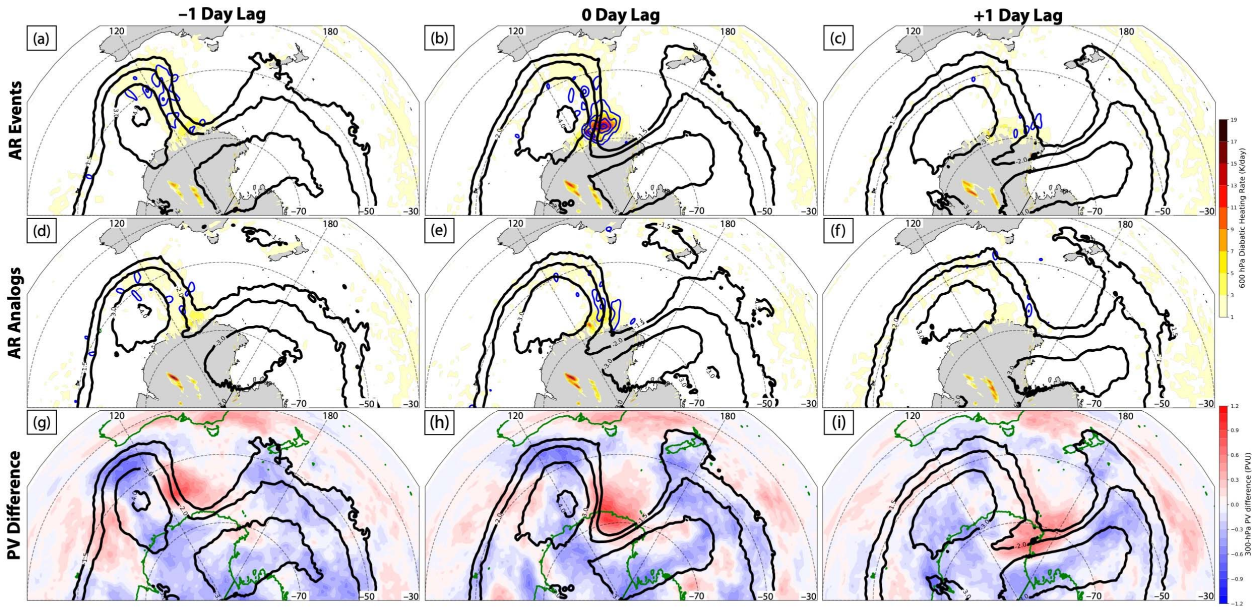

Figure 6. Composite of 300 hPa PV (black contours), 600 hPa diabatic heating (shading), and 400 hPa anticyclonic PV tendencies due to diabatic heating (blue contours) for (a) AR events and (d) non-AR analogue events one day prior to AR landfall. (g) The difference in 300 hPa PV between AR events and non-AR analogues (shading), with the 300 hPa PV from AR events overlaid in black contours. (b,e,h), as in (a,d,g) but at the time of AR landfall, and (c,f,i), as in (a,d,g), but for a +1 day lag.

The composite PV distribution during AR events also exhibits a filament of smaller PV values that wraps cyclonically poleward of DDU, characteristic of a cyclonic wave-breaking event (e.g., Thorncroft et al., 1993). Cyclonic wave-breaking often serves as a precursor to the development of blocking events that can favor the occurrence of sequentially-linked AR landfalls near DDU over a short period of time (e.g., Fish et al., 2019; Maclennan et al., 2023). Last, positive PV differences between the AR and non-AR analogues are noted along the eastern flank of the upper-tropospheric trough near DDU, indicating that the flow tends to be more progressive during non-AR analogues, supporting the Hovmoller analysis from Figure 5. The persistence of the upper-tropospheric trough-ridge couplet near DDU during AR events is favorable for the continued production of condensation and precipitation in the vicinity of DDU via the persistence of synoptic-scale forcing for surface cyclogenesis and vertical motion over the region.

To differentiate between atmospheric ridges and blocking during AR events, the Pook blocking index from Pook et al., (2013) was adapted for Antarctica with composite indices calculated for ARs and the non-AR analogues. Figure S4 shows a spatial example of the Pook blocking index for a case study discussed in the next section. By focusing on days within previously identified weather regimes that favored AR transport towards DDU (see regime pattern #7, #9, #10, and #11 in Figure 2 of Pohl et al., 2021), we determined that blocking intensity was greater overall for AR events compared to non-AR analogues, despite the two sharing common geopotential height patterns (Figure 7). The regimes that coincide with AR events show regions of high blocking indices around one day before the AR landfall. Variations in the longitude of the blocking index maxima between weather regimes reflect the various positions of the resultant ridge with regime #9 and #11 positioning the downstream ridge farthest east (Figures 7a, 7d, 7g, and 7j). Thus, even though the longitude remains unchanged between AR and non-AR analogues within each regime, the main difference between both groups of days is the intensity of the blocking index, as well as corresponding geopotential height anomalies (Figure S1), which form environments more favorable for poleward geostrophic transport for the AR cases.

When comparing the blocking patterns between ARs and their non-AR analogues, a distinct pattern emerges. Not only do the AR events have higher blocking indices, the greatest differences are concentrated east of DDU (140°), and tend to occur between the landfall time and one day after landfall, especially for regime #7 and #11 (Figures 7c, 7f, 7i , and 7l). While the 5-day running mean used for calculating the blocking index can obscure daily differences, the results in Figure 7 are likely a reflection of the enhanced 3D advection and diabatic production PV within AR environments leading to ridge amplification (Zhang & Wang, 2018). Thus, AR events likely feature a short-term positive feedback with the downstream ridge, with each feature enhancing the magnitude of the other.

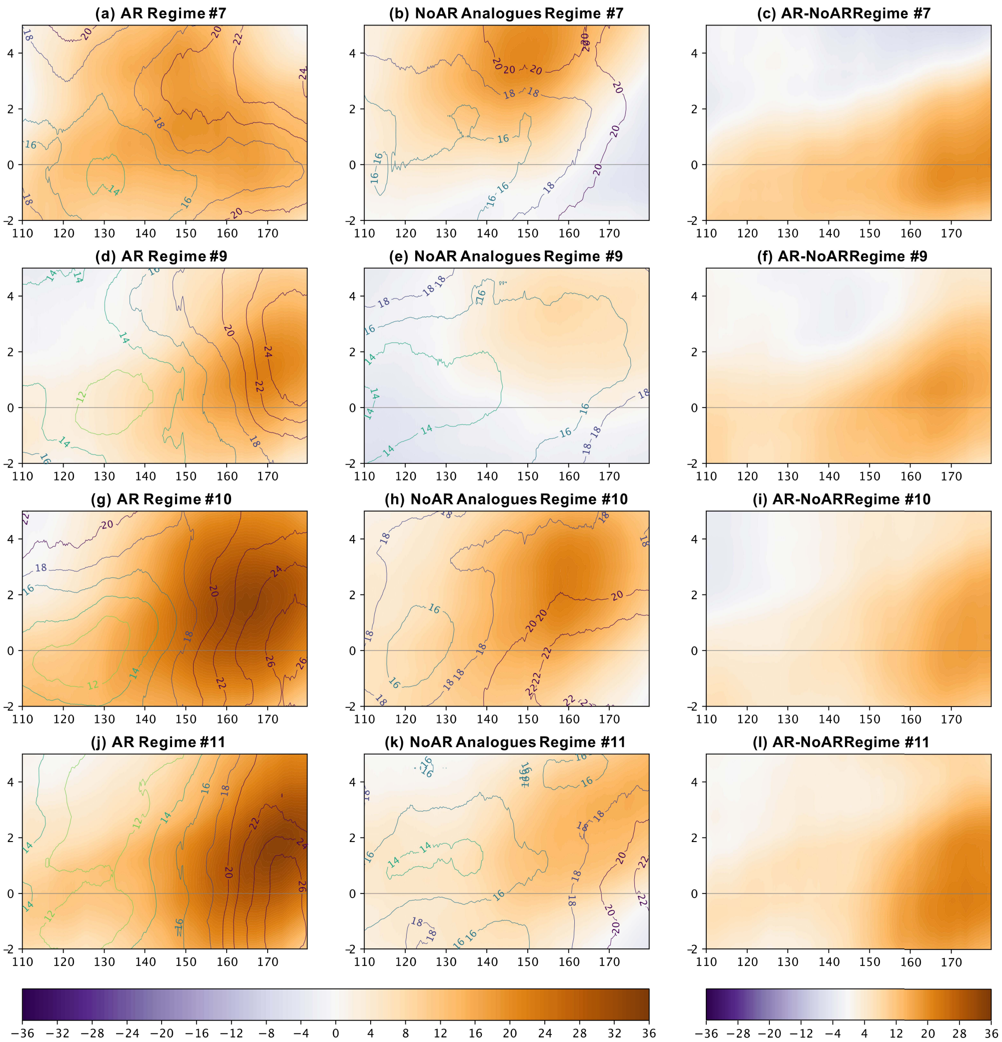

Figure 7. Longitude-time diagrams of the Pook blocking indices (Pook et al., 2013) for the 4 weather regimes most conducive to ARs in the DDU region (#7, 9, 10, 11: Pohl et al. 2021)during AR days (left column), non-AR analogues (middle column), and the differences between AR days and the non-AR analogues (right column). For the first two columns, colors indicate the composite mean BI (see color scale) and contours show the corresponding standard deviations. For the third column, colors indicate the BL differences. The x-axes are centered on the longitude of DDU (140°) and the y-axis show lags (in days) before (negative values) and after (positive values) the AR landfall time (y=0).

3.3 January 2020 case study

Antarctic surface cyclones have been proven to be frequently associated with a TPV (Gordon et al., 2022). Since ARs are often attended by large cyclonic upper-level PV anomalies, these PV anomalies may reflect the influence of TPVs. To illustrate the potential influence of TPVs, and show how this influence aligns with various aspects of the AR dynamics discussed throughout the manuscript, we first present a case study of an AR event at DDU. From 21 -24 January 2020, DDU was affected by an AR family event (Fish et al., 2019; Maclennan et al., 2023) , with the first AR landfall occurring on 21 January and a second AR landfall occuring on the 24 January, which also happened to be the most intense AR to make landfall at DDU during the study period (1980 - 2020) according to the AR detection algorithm (Figure S3; max IVT 682 kg m^{-1} s^{-1}).

Figure 8 provides an overview of the various TPVs and surface cyclones involved with the 21 January AR (Figure 8a) and the 24 January AR (Figure 8b). The first AR event was associated with two TPVs (TPV1 and TPV2) that led to the development of the first surface cyclone (SC1; Figure 8a), while the second AR event was influenced by the interaction between three TPVs (TPV3, TPV4, and TPV5) and two surface cyclones (SC2 and SC3).

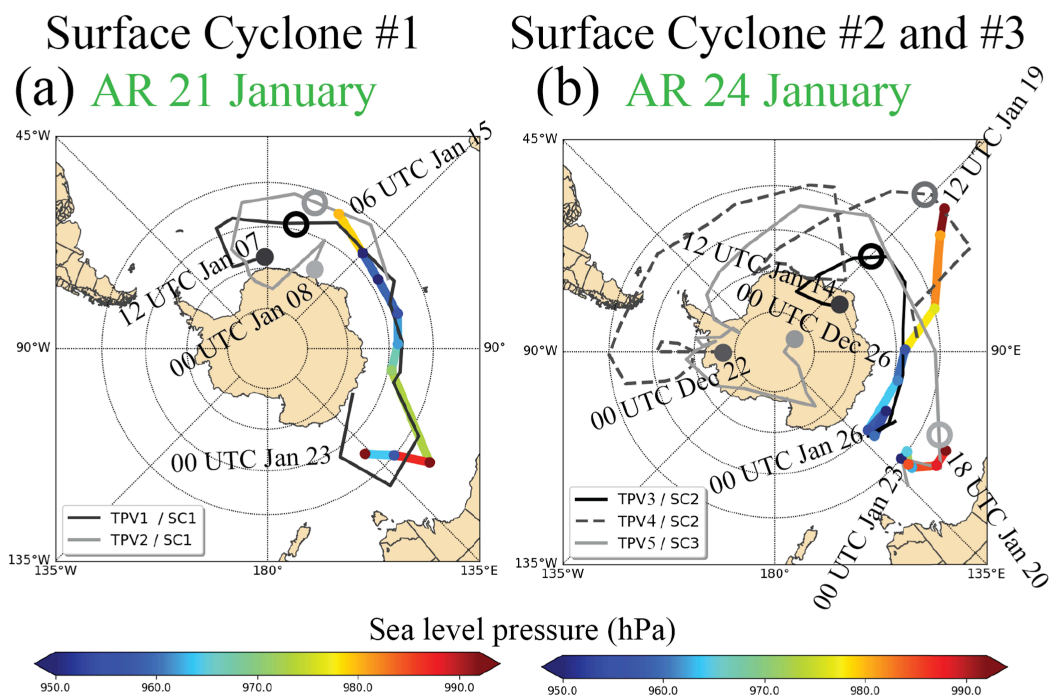

Figure 8. Tracks of the surface cyclones (color shaded by minimum sea level pressure in hPa) and their associated Tropopause Polar Vortices (TPVs) (black and gray lines) for the AR event at DDU on (a) 21 January and (b) 24 January 2020. Surface cyclone 1 (SC1) is denoted by the color shading in (a) while surface cyclone 2 (SC2) and surface cyclone 3 (SC3) is denoted by the color shading in (b). In (a), SC1 is associated with two TPVs: TPV1 denoted with a solid black line and TPV2 denoted with a solid gray line. In (b), SC2 is associated with three TPVs: TPV1 denoted with a solid black line, TPV2 denoted with a dashed dark gray line, and TPV3 denoted with a solid gray line while SC3 is associated with one TPV, TPV5 denoted with a solid light gray line. The filled circles and adjacent dates indicate the locations and dates where the TPVs were first identified. The open circles and adjacent dates indicate the locations and dates of the TPVs when first interacting with the associated surface cyclone.

Starting with the events leading to the 21 January AR landfall, both TPV1 and TPV2 formed near the Antarctic coastline near Dronning Maud Land on 7 January and 8 January, respectively, about one week prior to the development of SC1. SC1 specifically formed when it became collocated with TPV2 at around 53°S, 28°E on 15 January (Figure 8a); thereafter, TPV2 subsequently merged with TPV1 on 16 January. On 19 January, SC1 (Figure 9a) was located around 60°S, 90°E, and exhibits nearly an equivalent barotropic structure at this time with TPV1 stacked vertically on top of it. The highest poleward IVT values that affected DDU in association with SC1 occurred on 21 January when SC1 reintensified while interacting with TPV1 at its equatorward-most point near 43°S, 125°E (Figure 8a). Shortly thereafter, SC1 shifted poleward and merged with a new surface cyclone (SC3) near 50°S 130°E that formed from TPV5, which was propagating around the periphery of TPV1 and along the jet stream (Figure 9b). SC3 completely decayed by 23 January around 55°S, 137°E.

The passage of the first AR landfall on 21 January appears to have preconditioned the large-scale environment for the second, stronger AR landfall on 24 January. In particular, SC2 formed on 19 January well north of Antarctica around 38°S, 50°E, in association with TPV4 that developed nearly one month earlier on 22 December over the West Antarctic interior around 78°S 98°W (Figure 8b). SC2 began to intensify on 19 January near 40°S, 45°E, while it was located near the base of an amplified upper-level trough. SC2 further intensified rapidly while interacting with a different TPV (TPV3) off the coast near the Shackleton Ice Shelf and the Davis Sea on 21-22 January (cf. with Figure 9b). Meanwhile, SC3 formed in association with TPV5 and the decayed remains of SC1 at around 43°S, 120°E between Antarctica and Australia. A ridge between SC2 and SC3 amplified substantially at this time, directing moisture transport originating from subtropical regions towards high latitudes. The location of SC3 farther equatorward of SC2 at this time was likely an important factor in advecting high moisture across a large area spanning subtropical regions to the Antarctic farther downstream near DDU, as well. Due to the high amplitude of the upper-level Rossby wave pattern, both surface cyclones induce a strong stream of moisture (as indicated by poleward IVT) originating from the subtropics and reaching poleward of 60°S, near DDU. Just downstream of SC1 (at the end of its life on 23 January) and TPV1 (at around 150°E - 180°E), there is a block that has been nearly stationary since 14 January, as diagnosed by meridional winds on the dynamic tropopause (not shown) and seen in the Pook blocking index starting around 19 January (Figure S4) However, as the upstream flow continues to progress eastward into the blocked flow region, the high-amplitude ridge narrows longitudinally and exhibits a shape characteristic of a cyclonic Rossby wave breaking event between SC2 and SC3 causing a rapid decay of SC3 on 23 January (Figure 9c). Concurrently, SC2 strengthens to ~954 hPa near 60°S 120°E, with little eastward movement. The slow movement of this strong surface cyclone, and high amplitude of the upper-level flow pattern, has allowed a very strong AR to form, where moisture has ample time to be evaporated in the subtropics and transported towards DDU by 24 January (Figure 9c). The cyclonically curved poleward IVT and ridge pattern at the tropopause implies an enhanced upslope component of the lower-tropospheric flow along a large segment of the Antarctic coastline between 90°E - 165°E.

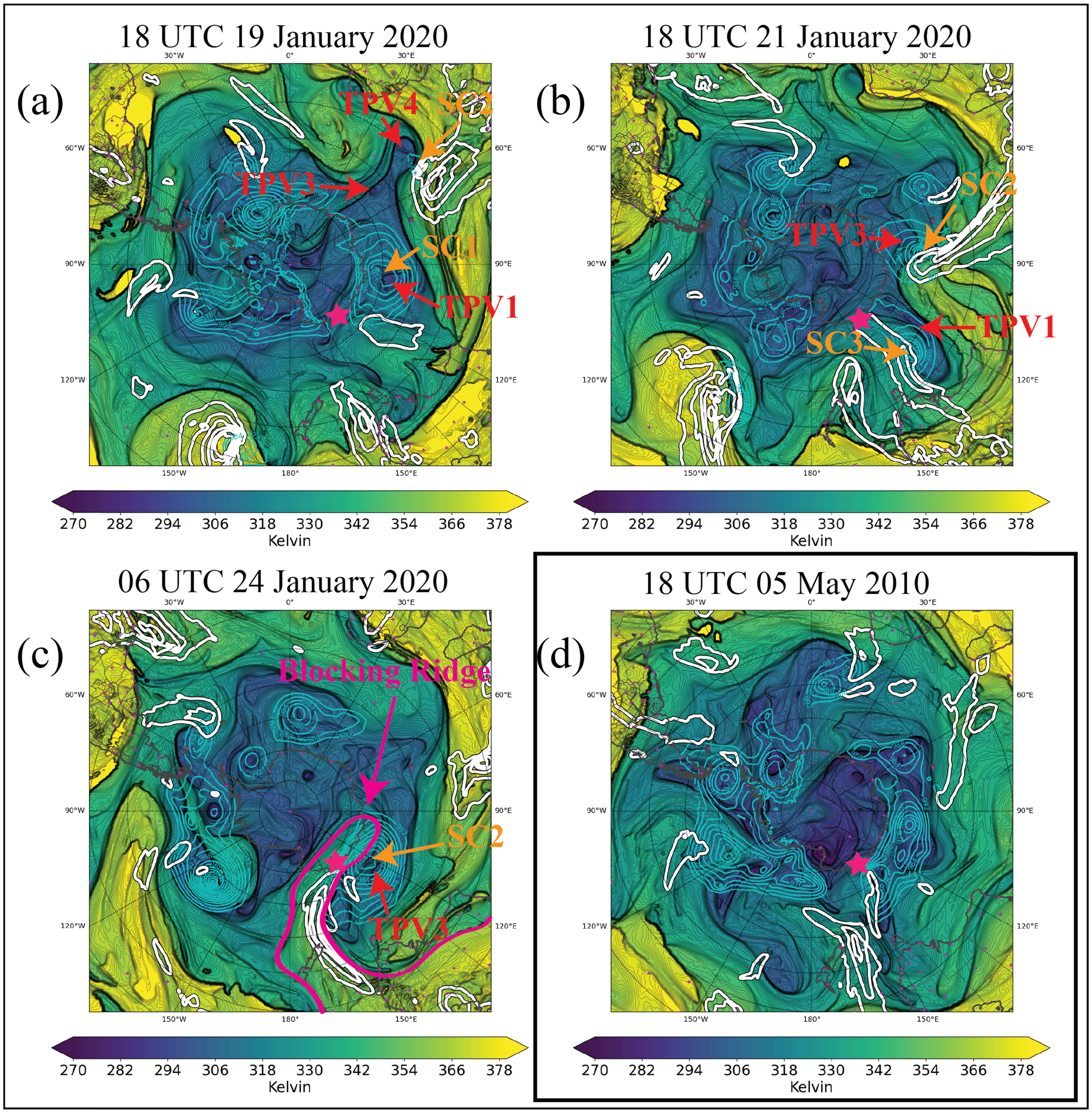

Figure 9. Potential temperature on the dynamic tropopause (K; color fill; contour interval 1 K), poleward integrated vapor transport (IVT) (kg m^{-1} s^{-1}; white contours; contour interval 300 kg m^{-1} s^{-1} beginning with 200 kg m^{-1} s^{-1}), and mean sea level pressure (hPa; blue contours; contour interval 4 hPa up to 992 hPa) on (a) 18 UTC 19 January, (b) 18 UTC 21 January, (c) 06 UTC 24 January 2020 and (d) 18 UTC 05 May 2010. The dynamic tropopause is taken here as the –2-PVU surface where 1 PVU = 1 x 10^{-6} K kg^{-1} s^{-2} m^2. The DDU station is denoted by the magenta star.

Note that three TPVs associated with these surface cyclones were quite long-lived, with lifetimes of at least 29-33 days. In fact, TPV5 was observed at least 25 days before the formation of SC3 and TPV4 was observed at least 28 days before the formation of SC2. This result is consistent with the precursory role of Antarctic TPVs on surface cyclone formation shown by Gordon et al., (2022). Looking at blocking indices based on the Pook blocking index, a high degree of blocking became established around DDU throughout the AR family event and extended 1-2 days beyond the 24 January AR landfall (Figure S4). The diabatic heat release from the initial AR landfall on 21 January likely intensified the poleward advection and amplification of anticyclonic PV at upper-levels, thus strengthening the block downstream of DDU. This strengthened block subsequently allowed for the second more powerful AR to be directed towards a similar part of the Antarctic coastline on 24 January. Looking at the non-AR analogue (18 UTC 05 May 2010) for the 24 January AR event shows several differences from the AR events from this case: (1) the lack of a cyclonically curved ridge at the tropopause, a disconnect between extratropical and tropical moisture streams, and a weaker extratropical cyclone and its attendant poleward IVT corridor (Figure 9d). The blocked flow pattern was also a likely factor that was important in providing sufficient time for moisture to move from the subtropics to the Antarctic during the AR family event.

4 Discussion and conclusion

ARs that impact DDU represent a subtropical to polar teleconnection where conditions at each stage of the AR life cycle mutually influence AR behavior and the large-scale atmospheric circulation. TPVs originating over the AIS may also represent a polar to subtropical teleconnection. Our proposed model for the AR life cycle in East Antarctica, summarized in Figure 10, begins with TPVs forming within favorable local environments over the AIS. These TPVs are then ejected equatorward and farther northward than the climatological storm track where they provide ideal dynamical conditions for surface cyclogenesis as coherent potential vorticity maxima on the tropopause (Cavallo & Hakim, 2009; Hakim, 2000). When TPVs are displaced far equatorward and in regions with large moisture reserves and combine with deep convection anomalies, a Rossby wave train can be excited and transport moisture towards the Antarctic continent (Clem et al., 2022; Röthlisberger et al., 2018). This moisture transport is enhanced through large surface evaporation, as evidenced by surface latent heat flux anomalies in the subtropics/mid-latitudes, and moves poleward in the form of an AR. Once the AR moves over the colder ocean waters closer to the Antarctic continent, condensation of the subtropical air masses and subsequent latent heat release as the moisture is isentropically lifted within the warm-conveyor belt contributes to the development of downstream anticyclonic PV tendencies at upper-levels and enhanced atmospheric blocking. The slower propagating group velocity of Rossby waves in the presence of blocking, along with cyclonic-wave breaking activity during AR events, can favor the occurrence of sequentially-linked AR landfalls or AR family events (Maclennan et al., 2023).

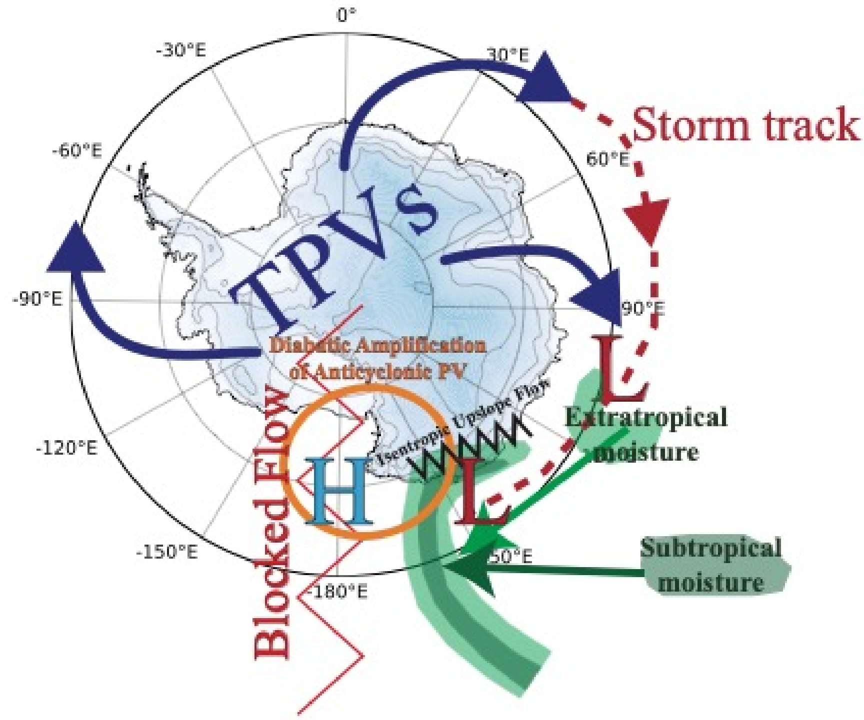

Figure 10. Schematic overview of ARs impacting DDU. The blue arrows represent typical pathways of TPVs and the dashed red contour represents typical pathways of extratropical cyclones along the storm track. The light green shadings represent moisture originating from extratropical cyclones while the dark green shadings represent moisture originating from the subtropics.

This model of the AR life cycle confirms many of the conclusions from the case study in Terpstra et al., (2021), such as the secondary cyclogenesis that occurs near the Antarctic coastline due to the effects from diabatic heating. As seen during the March 2022 extreme AR event, the moisture transport follows isentropic surfaces upwards within an attendant cyclone's warm-conveyor belt near the coastline, creating diabatic heating in the middle troposphere and anticyclonic PV tendencies at the tropopause (Dacre et al., 2019; Madonna et al., 2014; Terpstra et al., 2021; Wille et al., 2023a). The resulting secondary cyclogenesis could be induced via shortwave troughs propagating along the eastern edge of a broader longwave trough (Kingsmill et al., 2013), or as mesoscale frontal waves accompanying the AR (Martin et al., 2019), while also being influenced by the interaction with the katabatic winds while approaching the coastline (Bromwich et al., 2011). Clearly during AR events, the latent heat release from the moist air parcels being isentropically lifted, and the subsequent generation of downstream anticyclonic PV, is crucial for the atmospheric blocking maintenance (Pfahl et al., 2015; Steinfeld et al., 2020). Also, the positive feedback between ARs and downstream blocking can explain why extended periods of warm-air advection are often observed after the AR landfall has abated (Wille et al., 2019; Wille et al., 2023a). AR-related blocking can also trap subtropical air masses over the AIS, with enhanced downward longwave radiation from liquid-water clouds combining with downward shortwave radiation in cloud-breaks or porous cirrus layers to lead to intense, persistent positive temperature anomalies (Djoumna & Holland, 2021; Wille et al., 2019; Zou et al., 2021).

The use of analogues based on 700 hPa geopotential helps us describe what makes AR landfalls unique compared to other storms that might occur in East Antarctica. As ARs are often defined by IVT or IWV, basing their analogues on a different variable such as geopotential height describes the larger-scale environments in which ARs form and draws distinctions between similar non-AR environments to ultimately see how ARs influence their environment through diabatic heating. This provides insight on the connection between the variables that define ARs and the other variables they might influence. These analogues likely represent extratropical cyclones with reduced poleward moisture transport or even weaker ARs not detected by the algorithm, given this algorithm's relatively high threshold for detection (Collow et al., 2022). Still, the analogues demonstrate that the moisture transport accompanying ARs is an important factor that comprises these unique atmospheric circulation patterns. It is likely impossible to get the amplified jet pattern observed during ARs without the poleward moisture transport and the associated latent heat release/diabatic heating. Such a hypothesis could be verified via idealized modeling studies, but is outside of the scope of this work.

The exploration of the AR life cycle presented here for Adélie Land is not meant to represent an exhaustive, all-encompassing model of atmospheric dynamics related to Antarctic ARs, but instead an attempt to connect already established, yet disparate elements of AR dynamical research (see Baiman et al., 2023; Clem et al., 2022; Terpstra et al., 2021) and explain how AR-related moisture transport influences its surrounding dynamical environment. The elements described here would benefit from an Antarctic-wide examination to see if the process described here apply outside of East Antarctica. In particular, TPVs are a nascent topic of research around Antarctica (see Gordon et al., 2022) and this study is the first to connect TPVs and ARs anywhere in the world, albeit for just one case study. As TPVs are generated over the AIS and travel equatorward, they represent a connection between the local environment over Antarctica and cyclogenesis in the mid-latitudes, but further research is needed to quantify the co-occurrence rates between Antarctic ARs and TPVs . Finally, as ARs represent rare, high-impact events with large consequences for the AIS mass balance (Adusumilli et al., 2021; Gehring et al., 2022; I. V. Gorodetskaya et al., 2014; Maclennan et al., 2023; Michelle L. Maclennan et al., 2022; Simon et al., 2023; Wille et al., 2019, 2021, 2022), the results presented here highlight how climate change in the subtropics and mid-latitudes can translate to major impacts on the AIS.

Acknowledgments and data

We would like to thank Etienne Vignon for providing guidance on Antarctic atmospheric dynamics and Mike Pook for aiding in the adaptation of the Pook blocking index (Pook et al., 2013). J.D.W. and V.F. acknowledge support from the French Agence Nationale de la Recherche projects ANR-20-CE01-0013 (ARCA). We thank Michael Sprenger from the dynamic meteorology group at ETH for providing ERA5 potential vorticity on isentropic levels. T.R.V. and D.G.U acknowledge support from the Australian Research Council (DP220100606). A.C.W and R.B acknowledge support from the University of Colorado Boulder. K.R.C acknowledges funding from the Royal Society of New Zealand Marsden Fund grant MFP-VUW2010. The code

for the AR detection algorithm discussed in this paper is available at https://doi.org/10.5281/zenodo.7990215

References

Adusumilli, S., A. Fish, M., Fricker, H. A., & Medley, B. (2021). Atmospheric River Precipitation Contributed to Rapid Increases in Surface Height of the West Antarctic Ice Sheet in 2019. *Geophysical Research Letters*, *48*(5), e2020GL091076. https://doi.org/10.1029/2020GL091076

Baiman, R., Winters, A. C., Lenaerts, J., & Shields, C. A. (2023). Synoptic Drivers of Atmospheric River Induced Precipitation Near Dronning Maud Land, Antarctica. *Journal of Geophysical Research: Atmospheres*, *128*(7), e2022JD037859. https://doi.org/10.1029/2022JD037859

Benedict, J. J., Clement, A. C., & Medeiros, B. (2019). Atmospheric Blocking and Other Large-Scale Precursor Patterns of Landfalling Atmospheric Rivers in the North Pacific: A CESM2 Study. *Journal of Geophysical Research: Atmospheres*, *124*(21), 11330–11353. https://doi.org/10.1029/2019JD030790

Bluestein, H. B. (1992). Synoptic-dynamic meteorology in midlatitudes: Volume 1, principles of kinematics and dynamics. *Oxford University Press*.

Bozkurt, D., Rondanelli, R., Marín, J. C., & Garreaud, R. (2018). Foehn Event Triggered by an Atmospheric River Underlies Record-Setting Temperature Along Continental Antarctica. *Journal of Geophysical Research: Atmospheres*, *123*(8), 3871–3892. https://doi.org/10.1002/2017JD027796

Bray, M. T., & Cavallo, S. M. (2022). Characteristics of long-track tropopause polar vortices. *Weather and Climate Dynamics*, *3*(1), 251–278. https://doi.org/10.5194/wcd-3-251-2022

Bromwich, D. H., Steinhoff, D. F., Simmonds, I., Keay, K., & Fogt, R. L. (2011). Climatological aspects of cyclogenesis near Adélie Land Antarctica. *Tellus A: Dynamic Meteorology and Oceanography*, *63*(5), 921–938. https://doi.org/10.1111/j.1600-0870.2011.00537.x

Cavallo, S. M., & Hakim, G. J. (2009). Potential Vorticity Diagnosis of a Tropopause Polar Cyclone. *Monthly Weather Review*, *137*(4), 1358–1371. https://doi.org/10.1175/2008MWR2670.1

Cavallo, S. M., & Hakim, G. J. (2010). Composite Structure of Tropopause Polar Cyclones. *Monthly Weather Review*, *138*(10), 3840–3857. https://doi.org/10.1175/2010MWR3371.1

Cavallo, S. M., & Hakim, G. J. (2013). Physical Mechanisms of Tropopause Polar Vortex Intensity Change. *Journal of the Atmospheric Sciences*, *70*(11), 3359–3373. https://doi.org/10.1175/JAS-D-13-088.1

Clem, K. R., Bozkurt, D., Kennett, D., King, J. C., & Turner, J. (2022). Central tropical Pacific convection drives extreme high temperatures and surface melt on the Larsen C Ice Shelf, Antarctic Peninsula. *Nature Communications*, *13*(1), 3906. https://doi.org/10.1038/s41467-022-31119-4

Collow, A. B. M., Shields, C. A., Guan, B., Kim, S., Lora, J. M., McClenny, E. E., et al. (2022). An Overview of ARTMIP's Tier 2 Reanalysis Intercomparison: Uncertainty in the Detection of Atmospheric Rivers and Their Associated Precipitation. *Journal of Geophysical Research: Atmospheres*, *127*(8), e2021JD036155. https://doi.org/10.1029/2021JD036155

Dacre, H. F., Martínez-Alvarado, O., & Mbengue, C. O. (2019). Linking Atmospheric Rivers and Warm Conveyor Belt Airflows. *Journal of Hydrometeorology*, *20*(6), 1183–1196. https://doi.org/10.1175/JHM-D-18-0175.1

Djoumna, G., & Holland, D. M. (2021). Atmospheric Rivers, Warm Air Intrusions, and Surface Radiation Balance in the Amundsen Sea Embayment. *Journal of Geophysical Research: Atmospheres*, *126*(13), e2020JD034119. https://doi.org/10.1029/2020JD034119

Ertel, H. (1942). Ein neuer hydrodynamischer Erhaltungssatz. *Naturwissenschaften*, *30*(36), 543–544. https://doi.org/10.1007/BF01475602

Favier, V., Krinner, G., Amory, C., Gallée, H., Beaumet, J., & Agosta, C. (2017). Antarctica-Regional Climate and Surface Mass Budget. *Current Climate Change Reports*. https://doi.org/10.1007/s40641-017-0072-z

Fish, M. A., Wilson, A. M., & Ralph, F. M. (2019). Atmospheric River Families: Definition and Associated Synoptic Conditions. *Journal of Hydrometeorology*, *20*(10), 2091–2108. https://doi.org/10.1175/JHM-D-18-0217.1

Gehring, J., Vignon, É., Billault-Roux, A.-C., Ferrone, A., Protat, A., Alexander, S. P., & Berne, A. (2022). Orographic Flow Influence on Precipitation During an Atmospheric River Event at Davis, Antarctica. *Journal of Geophysical Research: Atmospheres*, *127*(2), e2021JD035210. https://doi.org/10.1029/2021JD035210

González-Herrero, S., Barriopedro, D., Trigo, R. M., López-Bustins, J. A., & Oliva, M. (2022). Climate warming amplified the 2020 record-breaking heatwave in the Antarctic Peninsula. *Communications Earth & Environment*, *3*(1), 122. https://doi.org/10.1038/s43247-022-00450-5

Gordon, A. E., Cavallo, S. M., & Novak, A. K. (2022). Evaluating Common Characteristics of Antarctic Tropopause Polar Vortices. *Journal of the Atmospheric Sciences*. https://doi.org/10.1175/JAS-D-22-0091.1

Gorodetskaya, I. V., Durán-Alarcón, C., Gonzalez-Herrero, S., Clem, K., Imazio, P. R., Santos,

C. L.-D., et al. (2023). *Compound drivers behind new record high temperatures and surface melt at the Antarctic Peninsula in February 2022* (preprint). In Review. https://doi.org/10.21203/rs.3.rs-2544063/v1

Gorodetskaya, I. V., Tsukernik, M., Claes, K., Ralph, M. F., Neff, W. D., & Van Lipzig, N. P. M. (2014). The role of atmospheric rivers in anomalous snow accumulation in East Antarctica. *Geophysical Research Letters*, *41*(17), 6199–6206. https://doi.org/10.1002/2014GL060881

Gutiérrez, J. M., Jones, R. G., Narisma, G. T., Alves, L. M., Amjad, M., Gorodetskaya, I. V., et al. (2021). Atlas. In V. Masson-Delmotte, P. Zhai, A. Pirani, S. L. Connors, C. Péan, S. Berger, et al. (Eds.). *Climate Change 2021 – The Physical Science Basis: Working Group I Contribution to the Sixth Assessment Report of the Intergovernmental Panel on Climate Change* (1st ed.). Cambridge University Press. https://doi.org/10.1017/9781009157896

Hakim, G. J. (2000). Climatology of Coherent Structures on the Extratropical Tropopause. *Monthly Weather Review*, *128*(2), 385–406. https://doi.org/10.1175/1520-0493(2000)128<0385:COCSOT>2.0.CO;2

Harrold, T. W. (1973). Mechanisms influencing the distribution of precipitation within baroclinic disturbances. *Quarterly Journal of the Royal Meteorological Society*, *99*(420), 232–251. https://doi.org/10.1002/qj.49709942003

Hauser, S., Teubler, F., Riemer, M., Knippertz, P., & Grams, C. M. (2023). Towards a holistic understanding of blocked regime dynamics through a combination of complementary diagnostic perspectives. *Weather and Climate Dynamics*, *4*(2), 399–425. https://doi.org/10.5194/wcd-4-399-2023

Hersbach, H., Bell, B., Berrisford, P., Hirahara, S., Horányi, A., Muñoz-Sabater, J., et al. (2020).

The ERA5 global reanalysis. *Quarterly Journal of the Royal Meteorological Society*, *146*(730), 1999–2049. https://doi.org/10.1002/qj.3803

Hirasawa, N., Nakamura, H., Motoyama, H., Hayashi, M., & Yamanouchi, T. (2013). The role of synoptic-scale features and advection in prolonged warming and generation of different forms of precipitation at Dome Fuji station, Antarctica, following a prominent blocking event. *Journal of Geophysical Research: Atmospheres*, *118*(13), 6916–6928. https://doi.org/10.1002/jgrd.50532

Hoskins, B. J., & Hodges, K. I. (2005). A New Perspective on Southern Hemisphere Storm Tracks. *Journal of Climate*, *18*(20), 4108–4129. https://doi.org/10.1175/JCLI3570.1

Hoskins, B. J., McIntyre, M. E., & Robertson, A. W. (1985). On the use and significance of isentropic potential vorticity maps. *Quarterly Journal of the Royal Meteorological Society*, *111*(470), 877–946. https://doi.org/10.1002/qj.49711147002

Jullien, N., Vignon, É., Sprenger, M., Aemisegger, F., & Berne, A. (2020). Synoptic conditions and atmospheric moisture pathways associated with virga and precipitation over coastal Adélie Land in Antarctica. *The Cryosphere*, *14*(5), 1685–1702. https://doi.org/10.5194/tc-14-1685-2020

King, J. C., & Turner, J. (2007). *Antarctic Meteorology and Climatology*. Cambridge University Press.

Kingsmill, D. E., Neiman, P. J., Moore, B. J., Hughes, M., Yuter, S. E., & Ralph, F. M. (2013). Kinematic and Thermodynamic Structures of Sierra Barrier Jets and Overrunning Atmospheric Rivers during a Landfalling Winter Storm in Northern California. *Monthly Weather Review*, *141*(6), 2015–2036. https://doi.org/10.1175/MWR-D-12-00277.1

Kittel, C., Amory, C., Agosta, C., Jourdain, N. C., Hofer, S., Delhasse, A., et al. (2021).

Diverging future surface mass balance between the Antarctic ice shelves and grounded ice sheet. *The Cryosphere*, *15*(3), 1215–1236. https://doi.org/10.5194/tc-15-1215-2021

Lackmann, G. M. (2002). Cold-Frontal Potential Vorticity Maxima, the Low-Level Jet, and Moisture Transport in Extratropical Cyclones. *Monthly Weather Review*, *130*(1), 59–74. https://doi.org/10.1175/1520-0493(2002)130<0059:CFPVMT>2.0.CO;2

Liang, K., Wang, J., Luo, H., & Yang, Q. (2023). The Role of Atmospheric Rivers in Antarctic Sea Ice Variations. *Geophysical Research Letters*, *50*(8), e2022GL102588. https://doi.org/10.1029/2022GL102588

Ligtenberg, S. R. M., van de Berg, W. J., van den Broeke, M. R., Rae, J. G. L., & van Meijgaard, E. (2013). Future surface mass balance of the Antarctic ice sheet and its influence on sea l evel change, simulated by a regional atmospheric climate model. *Climate Dynamics*, *41*(3–4), 867–884. https://doi.org/10.1007/s00382-013-1749-1

Lillo, S. P., Cavallo, S. M., Parsons, D. B., & Riedel, C. (2021). The Role of a Tropopause Polar Vortex in the Generation of the January 2019 Extreme Arctic Outbreak. *Journal of the Atmospheric Sciences*, *78*(9), 2801–2821. https://doi.org/10.1175/JAS-D-20-0285.1

Ling, J., & Zhang, C. (2013). Diabatic Heating Profiles in Recent Global Reanalyses. *Journal of Climate*, *26*(10), 3307–3325. https://doi.org/10.1175/JCLI-D-12-00384.1

Maclennan, M. L., Lenaerts, J. T. M., Shields, C. A., Hoffman, A. O., Wever, N., Thompson-Munson, M., et al. (2023). Climatology and surface impacts of atmospheric rivers on West Antarctica. *The Cryosphere*, *17*(2), 865–881. https://doi.org/10.5194/tc-17-865-2023

Maclennan, M. L., & Lenaerts, J. T. M. (2021). Large-Scale Atmospheric Drivers of

Snowfall Over Thwaites Glacier, Antarctica. *Geophysical Research Letters*, *48*(17), e2021GL093644. https://doi.org/10.1029/2021GL093644

Maclennan, M. L., Lenaerts, J. T. M., Shields, C., & Wille, J. D. (2022). Contribution of Atmospheric Rivers to Antarctic Precipitation. *Geophysical Research Letters*, *49*(18), e2022GL100585. https://doi.org/10.1029/2022GL100585

Madonna, E., Wernli, H., Joos, H., & Martius, O. (2014). Warm Conveyor Belts in the ERA-Interim Dataset (1979–2010). Part I: Climatology and Potential Vorticity Evolution. *Journal of Climate*, *27*(1), 3–26. https://doi.org/10.1175/JCLI-D-12-00720.1

Martin, A. C., Ralph, F. M., Wilson, A., DeHaan, L., & Kawzenuk, B. (2019). Rapid Cyclogenesis from a Mesoscale Frontal Wave on an Atmospheric River: Impacts on Forecast Skill and Predictability during Atmospheric River Landfall. *Journal of Hydrometeorology*, *20*(9), 1779–1794. https://doi.org/10.1175/JHM-D-18-0239.1

Massom, R. A., Pook, M. J., Comiso, J. C., Adams, N., Turner, J., Lachlan-Cope, T., & Gibson, T. T. (2004). Precipitation over the Interior East Antarctic Ice Sheet Related to Midlatitude Blocking-High Activity. *Journal of Climate*, *17*(10), 1914–1928. https://doi.org/10.1175/1520-0442(2004)017<1914:POTIEA>2.0.CO;2

Mattingly, K. S., Turton, J. V., Wille, J. D., Noël, B., Fettweis, X., Rennermalm, Å. K., & Mote, T. L. (2023). Increasing extreme melt in northeast Greenland linked to foehn winds and atmospheric rivers. *Nature Communications*, *14*(1), 1743. https://doi.org/10.1038/s41467-023-37434-8

Mottram, R., Hansen, N., Kittel, C., van Wessem, J. M., Agosta, C., Amory, C., et al. (2021).

What is the surface mass balance of Antarctica? An intercomparison of regional climate model estimates. *The Cryosphere*, *15*(8), 3751–3784. https://doi.org/10.5194/tc-15-3751-2021

Nakamura, N., & Huang, C. S. Y. (2018). Atmospheric blocking as a traffic jam in the jet stream. *Science*, *361*(6397), 42–47. https://doi.org/10.1126/science.aat0721

Nash, D., Waliser, D., Guan, B., Ye, H., & Ralph, F. M. (2018). The Role of Atmospheric Rivers in Extratropical and Polar Hydroclimate. *Journal of Geophysical Research: Atmospheres*, *123*(13), 6804–6821. https://doi.org/10.1029/2017JD028130

Nicolas, J. P., & Bromwich, D. H. (2011). Climate of West Antarctica and Influence of Marine Air Intrusions. *Journal of Climate*, *24*(1), 49–67. https://doi.org/10.1175/2010JCLI3522.1

Pfahl, S., Schwierz, C., Croci-Maspoli, M., Grams, C. M., & Wernli, H. (2015). Importance of latent heat release in ascending air streams for atmospheric blocking. *Nature Geoscience*, *8*(8), 610–614. https://doi.org/10.1038/ngeo2487

Pohl, B., Favier, V., Wille, J., Udy, D. G., Vance, T. R., Pergaud, J., et al. (2021). Relationship Between Weather Regimes and Atmospheric Rivers in East Antarctica. *Journal of Geophysical Research: Atmospheres*, *126*(24), e2021JD035294. https://doi.org/udy

Pook, M. J., Risbey, J. S., McIntosh, P. C., Ummenhofer, C. C., Marshall, A. G., & Meyers, G. A. (2013). The Seasonal Cycle of Blocking and Associated Physical Mechanisms in the Australian Region and Relationship with Rainfall. *Monthly Weather Review*, *141*(12), 4534–4553. https://doi.org/10.1175/MWR-D-13-00040.1

Ralph, F. M., Neiman, P. J., & Wick, G. A. (2004). Satellite and CALJET Aircraft Observations of Atmospheric Rivers over the Eastern North Pacific Ocean during the Winter of 1997/98. *Monthly Weather Review*, *132*(7), 1721–1745. https://doi.org/10.1175/1520-0493(2004)132<1721:SACAOO>2.0.CO;2

Reeves, H. D., & Lackmann, G. M. (2004). An Investigation of the Influence of Latent Heat Release on Cold-Frontal Motion. *Monthly Weather Review*, *132*(12), 2864–2881. https://doi.org/10.1175/MWR2827.1

Rignot, E., Mouginot, J., Scheuchl, B., van den Broeke, M., van Wessem, M. J., & Morlighem, M. (2019). Four decades of Antarctic Ice Sheet mass balance from 1979–2017. *Proceedings of the National Academy of Sciences*, *116*(4), 1095. https://doi.org/10.1073/pnas.1812883116

Röthlisberger, M., Martius, O., & Wernli, H. (2018). Northern Hemisphere Rossby Wave Initiation Events on the Extratropical Jet—A Climatological Analysis. *Journal of Climate*, *31*(2), 743–760. https://doi.org/10.1175/JCLI-D-17-0346.1

Rutz, J. J., Shields, C. A., Lora, J. M., Payne, A. E., Guan, B., Ullrich, P., et al. (2019). The Atmospheric River Tracking Method Intercomparison Project (ARTMIP): Quantifying Uncertainties in Atmospheric River Climatology. *Journal of Geophysical Research: Atmospheres*, *124*(24), 13777–13802. https://doi.org/10.1029/2019JD030936

Schlosser, E., Manning, K. W., Powers, J. G., Duda, M. G., Birnbaum, G., & Fujita, K. (2010). Characteristics of high-precipitation events in Dronning Maud Land, Antarctica. *Journal of Geophysical Research*, *115*(D14), D14107. https://doi.org/10.1029/2009JD013410

Scott, R. C., Nicolas, J. P., Bromwich, D. H., Norris, J. R., & Lubin, D. (2019). Meteorological Drivers and Large-Scale Climate Forcing of West Antarctic Surface Melt. *Journal of Climate*, *32*(3), 665–684. https://doi.org/10.1175/JCLI-D-18-0233.1

Shields, C. A., Wille, J. D., Marquardt Collow, A. B., Maclennan, M., & Gorodetskaya, I. V. (2022). Evaluating Uncertainty and Modes of Variability for Antarctic Atmospheric Rivers. *Geophysical Research Letters*, *49*(16), e2022GL099577. https://doi.org/10.1029/2022GL099577

Simmonds, I., Keay, K., & Lim, E.-P. (2003). Synoptic Activity in the Seas around Antarctica. *Monthly Weather Review*, *131*(2), 272–288. https://doi.org/10.1175/1520-0493(2003)131<0272:SAITSA>2.0.CO;2

Simon, S., Turner, J., Thamban, M., Wille, J., & Deb, P. (2023). Spatiotemporal variability of extreme precipitation events and associated atmospheric processes over Dronning Maud Land, East Antarctica. https://doi.org/10.22541/essoar.168121508.85938968/v1

Sinclair, V. A., & Dacre, H. F. (2019). Which Extratropical Cyclones Contribute Most to the Transport of Moisture in the Southern Hemisphere? *Journal of Geophysical Research: Atmospheres*, *124*(5), 2525–2545. https://doi.org/10.1029/2018JD028766

Sodemann, H., & Stohl, A. (2013). Moisture Origin and Meridional Transport in Atmospheric Rivers and Their Association with Multiple Cyclones. *Monthly Weather Review*, *141*(8), 2850–2868. https://doi.org/10.1175/MWR-D-12-00256.1

Steinfeld, D., Boettcher, M., Forbes, R., & Pfahl, S. (2020). The sensitivity of atmospheric blocking to upstream latent heating – numerical experiments. *Weather and Climate Dynamics*, *1*(2), 405–426. https://doi.org/10.5194/wcd-1-405-2020

Szapiro, N., & Cavallo, S. M. (2018). TPVTrack (v1.0): A watershed segmentation and overlap correspondence method for tracking tropopause polar vortices. *Geoscientific Model Development*, *11*(12), 5173–5187.

Tamarin, T., & Kaspi, Y. (2016). The Poleward Motion of Extratropical Cyclones from a

Potential Vorticity Tendency Analysis. *Journal of the Atmospheric Sciences*, *73*(4), 1687–1707. https://doi.org/10.1175/JAS-D-15-0168.1

Terpstra, A., Gorodetskaya, I. V., & Sodemann, H. (2021). Linking Sub-Tropical Evaporation and Extreme Precipitation Over East Antarctica: An Atmospheric River Case Study. *Journal of Geophysical Research: Atmospheres*, *126*(9), e2020JD033617. https://doi.org/10.1029/2020JD033617

Thorncroft, C. D., Hoskins, B. J., & McIntyre, M. E. (1993). Two paradigms of baroclinic-wave life-cycle behaviour. *Quarterly Journal of the Royal Meteorological Society*, *119*(509), 17–55. https://doi.org/10.1002/qj.49711950903

Turner, J., Lu, H., King, J. C., Carpentier, S., Lazzara, M., Phillips, T., & Wille, J. (2022). An Extreme High Temperature Event in Coastal East Antarctica Associated With an Atmospheric River and Record Summer Downslope Winds. *Geophysical Research Letters*, *49*(4), e2021GL097108. https://doi.org/10.1029/2021GL097108

Udy, D. G., Vance, T. R., Kiem, A. S., Holbrook, N. J., & Curran, M. A. J. (2021). Links between Large-Scale Modes of Climate Variability and Synoptic Weather Patterns in the Southern Indian Ocean. *Journal of Climate*, *34*(3), 883–899. https://doi.org/10.1175/JCLI-D-20-0297.1

Wille, J. D., Favier, V., Dufour, A., Gorodetskaya, I. V., Turner, J., Agosta, C., & Codron, F. (2019). West Antarctic surface melt triggered by atmospheric rivers. *Nature Geoscience*, *12*(11), 911–916. https://doi.org/10.1038/s41561-019-0460-1

Wille, J. D., Favier, V., Gorodetskaya, I. V., Agosta, C., Kittel, C., Beeman, J. C., et al. (2021).

Antarctic Atmospheric River Climatology and Precipitation Impacts. *Journal of Geophysical Research: Atmospheres*, *126*(8), e2020JD033788. https://doi.org/10.1029/2020JD033788

Wille, J. D., Favier, V., Jourdain, N. C., Kittel, C., Turton, J. V., Agosta, C., et al. (2022). Intense atmospheric rivers can weaken ice shelf stability at the Antarctic Peninsula. *Communications Earth & Environment*, *3*(1), 90. https://doi.org/10.1038/s43247-022-00422-9

Wille, J. D., and CoAuthors (East Antarctica Heatwave Team), 2023a:. The extraordinary March 2022 East Antarctica "heat" wave. Part 1: observations and meteorological drivers. *Journal of Climate*, Submitted

Wille, J. D., and CoAuthors (The East Antarctica Heatwave Team), 2023b: The extraordinary March 2022 East Antarctica "heat" wave. Part 2: impacts on the Antarctic ice sheet. *Journal of Climate*, Submitted

Xu, M., Yu, L., Liang, K., Vihma, T., Bozkurt, D., Hu, X., & Yang, Q. (2021). Dominant role of vertical air flows in the unprecedented warming on the Antarctic Peninsula in February 2020. *Communications Earth & Environment*, *2*(1), 133. https://doi.org/10.1038/s43247-021-00203-w

Zhang, G., & Wang, Z. (2018). North Atlantic Extratropical Rossby Wave Breaking during the Warm Season: Wave Life Cycle and Role of Diabatic Heating. *Monthly Weather Review*, *146*(3), 695–712. https://doi.org/10.1175/MWR-D-17-0204.1

Zhu, Y., & Newell, R. E. (1994). Atmospheric rivers and bombs. *Geophysical Research Letters*, *21*(18), 1999–2002. https://doi.org/10.1029/94GL01710

Zhu, Y., & Newell, R. E. (1998). A Proposed Algorithm for Moisture Fluxes from Atmospheric

Rivers. *Monthly Weather Review*, *126*(3), 725–735. https://doi.org/10.1175/1520-0493(1998)126<0725:APAFMF>2.0.CO;2

Zou, X., Bromwich, D. H., Montenegro, A., Wang, S.-H., & Bai, L. (2021). Major surface melting over the Ross Ice Shelf part II: Surface energy balance. *Quarterly Journal of the Royal Meteorological Society*, *147*(738), 2895–2916. https://doi.org/10.1002/qj.4105